Characterization of aerosol properties during a huge transatlantic smoke transport event ~~by constructing an Aeolus smoke dataset~~using Aeolus observations in synergy with multi-platform data

Kangwen Sun[1,2], Guangyao Dai[1], Dimitri Trapon[2], Holger Baars[2], Albert Ansmann[2], Ulla Wandinger[2], Songhua Wu[1,3,4]

[1]College of Marine Technology, Faculty of Information Science and Engineering, Ocean University of China, Qingdao, China
[2]Leibniz Institute for Tropospheric Research (TROPOS), Leipzig, Germany
[3]Laoshan Laboratory, Qingdao, China
[4]Institute for Advanced Ocean Study, Ocean University of China, Qingdao, China

Correspondence to: Songhua Wu (wush@ouc.edu.cn)

Abstract. During the wildfire season on the West Coast of the US in September 2020, biomass burning smoke aerosols were continually generated, resulting in several transatlantic transport events~~s~~. As a high spectral resolution lidar (HSRL), ALADIN could directly retrieve the aerosol extinction and backscatter coefficient. Targeting a large-scale tropospheric smoke transport event originating from the western US on 14 September and arriving over Europe on 21 September, a method for constructing an Aeolus smoke dataset was developed based on ALADIN observations, in synergy with multi-source data. ~~The backscatter coefficient in the smoke dataset was corrected using a linear depolarization ratio of 0.15, since ALADIN detected only co-polarized backscattered signals and the averaged smoke depolarization ratio remained relatively stable throughout the transport.~~ Utilizing selected cross-sections from this dataset, the vertical structure of the smoke layers at different transport stages are presented. HYSPLIT simulations support the representativeness of these layers across the transport. Statistical analyses of the complete Aeolus smoke dataset from 14 to 21 September reveal the evolution of the smoke plume throughout its transatlantic pathway. The dense smoke plume across the transport is characterized by mean extinction coefficients of approximately 200 Mm^{-1} of across all the selected cross-sections and a decline in AOD from 0.54 to 0.33 along the transport path. The smoke layers ascended from approximately 4.4 km above the US to over 6 km above the Europe and appeared above clouds upon reaching Europe. The initially decreasing and then increasing lidar ratios indicate the aging process and hygroscopic growth of smoke particles. Plume separation was observed over the mid-Atlantic, and the two resulting branches were investigated individually. To our knowledge, this paper presents the first use of a spaceborne HSRL for observations and analyses of a large-scale tropospheric smoke transport. The comprehensive characterization presented herein provides valuable information for advancing global aerosol research.

1 Introduction

Smoke aerosols, primarily produced by biomass burning events such as wildfires, exert significant impacts on the Earth system by perturbing the radiation balance, influencing cloud formation, and degrading air quality (Sokolik et al., 2019; Ditas et al., 2018; Hirsch & Koren, 2021). In recent years, climate change has driven hotter and drier conditions and more frequent wildfires, leading to the formation of increasingly intense smoke layers in the atmosphere (Kirchmeier-Young et al., 2019; Cunningham et al., 2024; Trickl et al., 2024). Smoke aerosols from wildfires can be lofted to altitudes of up to ~about 35 km, thereby inducing substantial perturbations to tropospheric cloud processes and stratospheric aerosol composition (Khaykin et al., 2020; Twohy et al., 2021; Peterson et al., 2021). Once injected, smoke plumes can undergo long-range transport via large-scale atmospheric circulation, affecting regions far from their sources. Accurately representing such long-range transport is therefore essential for the parameterization of cloud–aerosol interactions in regional and global models, ultimately improving the fidelity of weather and climate predictions (Lohmann and Neubauer, 2018; Beer et al., 2022, 2024).

Lidar remote sensing is an effective approach for atmospheric measurements, providing vertically resolved parameters and information. Based on ground-based lidar observations, extensive research has been conducted to investigate the characteristics of smoke aerosols and their environmental impacts. Using lidar measurements at Leipzig, Haarig et al. (2018) characterized the properties of aged tropospheric and stratospheric smoke originating from Canadian wildfires. The impacts of wildfire smoke aerosols on cirrus formation over the eastern Mediterranean and the Arctic were explored by Mamouri et al. (2023) and Ansmann et al. (2025), based on lidar observations. Wildfire smoke was found contributing to the processes driving record-breaking stratospheric ozone depletion over the Arctic and Antarctica in 2020 (Ohneiser et al., 2021). Therefore, with the observation records of single ground-based lidar station, 1) smoke plumes at specific phase of the whole development or transport process event can be characterized in detail, meanwhile 2) interactions between smoke layers and other atmospheric constituents, such as clouds or ozone, can be investigated. Furthermore, lidar networks, comprising multiple stations, have increasingly been employed in wildfire smoke research. Floutsi et al. (2023) derived universal lidar-based intensive optical properties of smoke aerosols - including the particle linear depolarization ratio, the extinction-to-backscatter ratio (lidar ratio), and the Ångström exponent - by analyzinganalysing long-term observations from the European Aerosol Research Lidar Network (EARLINET) and several dedicated campaigns (Pappalardo et al., 2014). Vaughan et al. (2018) and Baars et al. (2019) utilized the observations of the UK lidar network and the EARLINET individually, characterizing the smoke aerosols transported from North America. Although lidar sites can provide information on smoke over different regions, they primarily capture the decay phase of transport rather than the entire transport processevent. In summary, ground-based lidar stations and networks are valuable for investigating smoke processes over specific regions and for establishing comprehensive smoke databases, but they are limited in their ability to track long-range smoke transport.

For tracking long-distance smoke transport, particularly across oceans, satellite-based lidars provide valuable global measurements, as most operate in polar orbits and circle the Earth more than ten times per day. The Cloud-Aerosol Lidar with Orthogonal Polarization (CALIOP) aboard the Cloud-Aerosol Lidar and Infrared Pathfinder Satellite Observation (CALIPSO) mission measured global vertical profiles of atmospheric aerosol and cloud optical properties from 2006 to 2023 (Winker et al., 2009; Omar et al., 2009). Numerous transport studies exist based on CALIOP observation. For example, by u~~U~~sing three CALIOP measurement cross-sections, Vaughan et al. (2018) tracked a wildfire smoke plume originating in western Canada in May 2016 then~~ it~~ crossing~~ed~~ the Atlantic to the UK, finding that the plumes were primarily transported in the middle troposphere (3 to 11 km) with a slight ascending tendency, and that the smoke aerosol depolarization ratios at 532 nm remained below 0.1. Similarly, a wildfire smoke transport event from Canada to Europe in May - June 2019 was characterized by ~~analyzing~~analysing CALIOP profiles divided by west-to-east locations (Shang et al., 2024), revealing that 1) transport occurred mainly in the middle troposphere (3 to 8 km), 2) aerosol optical depth (AOD) at 532 nm decreased from 0.25 to near zero, and 3) depolarization ratio at 532 nm increased from 0.03 to 0.06. Focusing on smoke self-lofting, Ohneiser et al. (2023) examined CALIOP cross-sections of Canadian wildfire smoke in 2017 and Australian smoke in 2020, showing plumes lofted from 12 to 13 km to around 20 km ~~due to~~partly contributed by absorbing solar radiation, indicating the transports ~~were~~ took place in the upper troposphere and lower stratosphere. Collectively, these studies demonstrate that CALIOP measurements enable detailed tracking and characterization of long-range wildfire smoke transport. Nevertheless, as an elastic-backscatter lidar, CALIOP-derived extinction coefficients and AOD rely on assumptions of the extinction-to-backscatter ratio (lidar ratio) (Kim et al., 2018).

As the first wind spaceborne lidar and also the first operated spaceborne high spectral resolution lidar, the Atmospheric Laser Doppler Instrument (ALADIN) onboard Aeolus satellite measured global wind and aerosol profiles simultaneously for more than 4 years (August 2018 to April 2023) (Stoffelen et al., 2005; Reitebuch, 2012). The aerosol and cloud optical properties product (Level 2A) of Aeolus includes directly derived profiles of extinction coefficient and co-polarized backscatter coefficient ~~profiles~~ at 355 nm, because ALADIN transmits circularly polarized light but measures only the co-polarized component of the backscattered light (Flament et al., 2021). Aeolus Level 2A product has been involved in the research of the characterization of dust aerosols and the evaluation of the wind impact on marine aerosol (Song et al., 2024; Sun et al., 2024). It also provides opportunity to track and describe large-scale long-range aerosol transport with the underlying possible dynamic reasons described by the wind information. Based on Aeolus data, Dai et al. (2022) captured and analysed a huge dust transport event from the Sahara dust crossing the Atlantic to the Caribbean Sea occurred in June 2020. The dust plumes were found below 6 km during transport and the wind vector product (Level 2C) from Aeolus was also used to evaluate the transport intensity. ~~In this study,~~This study focuses on a huge smoke transport stage in September 2020~~ will be focused on~~, of which the smoke aerosols were generated from the extreme forest fires in California (Hu et al., 2022; Ceamanos et al., 2023; Eck et al., 2023). It has been reported that smoke plumes were transported across the Atlantic to Europe, with two distinct transport events identified, each lasting approximately 5–7 days.~~It has been reported that the smoke plumes were transported to Europe crossing Atlantic and the whole transport stage may include two distinct transport processes with the period of 5-7 days~~ (Hu et al., 2022). Aeolus Level 2A product has demonstrated the capability to measure smoke profiles (Baars et al., 2021). However, during long-range transport, smoke plumes may become mixed with other aerosols and clouds. Moreover, Aeolus's ability to classify aerosols and clouds was limited due to the absence of depolarization measurements. Based on Aeolus product, together with CALIOP, spaceborne passive instruments (Visible Infrared Imaging Radiometer Suite, VIIRS (Liu et al., 2014); Moderate-resolution Imaging Spectroradiometer, MODIS (Savtchenko et al., 2004)), models (Modern-Era Retrospective analysis for Research and Applications, Version 2, MERRA-2 (Gelaro et al., 2017; Buchard et al., 2017); Hybrid Single Particle Lagrangian Integrated Trajectory Model, HYSPLIT (Stein et al., 2015)), this study 1) determined the general region and period of the smoke transport, 2) derived the Aeolus smoke profiles and conducted validation, 3) selected the Aeolus cross-sections to characterize the smoke layers ~~in~~ at different transport ~~phases~~stages, and 4) investigated the features of the entire smoke event using all Aeolus smoke profiles in the transport region. The derived Aeolus smoke profiles dataset mainly include backscatter coefficient, extinction coefficient and lidar ratio.

The paper is organized as follows. Section 1 provides an introduction to the present study. Section 2 describes the data and models used. Section 3 localizes the targeted smoke transport event. Section 4 presents the methodology for developing and validating the Aeolus-based smoke dataset, along with the caveats and uncertainties encountered during the dataset development. Section 5 analyses and discusses the characterization of smoke aerosols across the transport, by examining cross-sections of the smoke aerosol layers at different transport stages, as well as the entire smoke plume throughout the transport process.~~The correction of backscatter coefficient was conducted using a linear depolarization ratio of 0.15 since the average smoke depolarization ratio remained relatively stable throughout the transport.~~

2 Data and model

2.1 ALADIN

During its operational lifetime from August 2018 to April 2023, the ALADIN instrument onboard the Aeolus satellite provided global atmospheric wind measurements along with aerosol and cloud observations simultaneously for more than 4 years, covering the atmospheric column from the surface to the lower stratosphere. As a high spectral resolution lidar operating at a wavelength of 354.8 nm, ALADIN had the capability to separate atmospheric particulate (aerosol and cloud) backscattered signal from molecular backscattered signal (Reitebuch et al., 2012). Thus, extinction coefficients can be retrieved directly without the need to assume a lidar ratio. However, ALADIN was not equipped with a cross-polar polarization detection channel, resulting in the absence of polarization information in its backscatter measurements (Flament et al., 2021). ALADIN operated on a dawn-dusk orbit with an inclination of 97.01°, and mean times of ascending/descending node at 18:00/6:00 (Local Time) (ESA, 2008). Further details on the instrument design and the measurement concept have been reported in Ansmann et al. (2007), Dabas et al. (2008), Flamant et al. (2008), Reitebuch (2012), Lux et al. (2020), and Flament et al. (2021).

Aeolus data products include several different levels: Level 0 (instrument housekeeping data), Level 1B (engineering-corrected HLOS winds), Level 2A (aerosol and cloud layer optical properties, including particulate extinction coefficient α, backscatter coefficient β, and lidar ratio, all at 355 nm), Level 2B (meteorologically representative HLOS winds) and Level 2C (Aeolus-assisted wind vectors) (Flamant et al., 2008; Tan et al., 2008; Rennie et al., 2020). "Baselines" of the products were defined to represent the products retrieved with different processor versions. Up to the time of this study, the products of Level 2A

Baseline 16 with the time period of Aeolus' whole lifetime have been published (https://aeolus-ds.eo.esa.int/oads/access/; last access: 27 August 2025). The Level 2A Baseline 16 product includes aerosol and cloud retrievals derived from various algorithms. Among them, the Standard Correct Algorithm (SCA) is a retrieval algorithm for particulate extinction and backscatter coefficient using a direct algebraic inversion scheme, and the SCAmid is a version using better vertical averaging strategy, of which the products were more recommended for usage than the initial one (Flament et al., 2021, Gkikas et al., 2023). The Mie Channel Algorithm MCA relies on Mie signal only and provides particle extinction coefficient assuming a fixed lidar ratio. The Maximum Likelihood Estimation (MLE) and the MLEsub algorithms, based on physically constrained optimal estimation, achieved more accurate~~found denoised~~ aerosol retrievals when compared to SCA and SCAmid, especially for the particle~~s~~ extinction coefficient (Ehlers et al., 2022; Trapon et al., 2025). The data with the MLEsub has higher horizontal resolution (18 km) than the one with the MLE (90 km). The AEL-PRO algorithm was developed targeting the Earth Cloud Aerosol and Radiation Explorer (EarthCARE) HSRL ATmospheric LIDar (ATLID), based on the feature mask identification as the previous step (Wang et al., 2024). More details of the Level 2A retrieval algorithm are introduced in the "ADM-Aeolus L2A Algorithm Theoretical Baseline Document" (Flamant et al., 2022). In this study, α and β in the Level 2A product with the MLE algorithm and aligned with 90 km horizontal from Baseline 16 were adopted. The MLE product was chosen because it integrates five times as many profiles as the MLEsub product, resulting in a higher signal-to-noise ratio and thus better data quality (Flamant et al., 2022). The vertical resolution varies from 0.25 km close to the surface to 2 km for top height, with most range bin thickness aligned with 0.5 km, 0.75 km and 1 km in upper troposphere. Relative humidity (RH) and molecular backscatter coefficient (β_m) from European Centre for Medium-Range Weather Forecasts Reanalysis 5 (ERA5) with the same grid of ~~Aeolus~~ ALADIN measurement data provided in the Aeolus Level 2A products are also used as the auxiliary data.

2.2 CALIOP

CALIOP on board CALIPSO measured global aerosol and cloud vertical profiles for around 17 years from June 2006 to June 2023. CALIOP Level 2 Aerosol Profile products provide directly retrieved backscatter coefficient at 532 nm and particulate depolarization ratio at 532 nm. In this study, the Aerosol Profile products of data version 4.21 were used to evaluate the stability of the depolarization ratio during the smoke transport. The vertical resolution of the Aerosol Profile products is variable in the altitude region of 0.5 km to 30.1 km: 60 m for -0.5 km to 20.2 km, 180 m for 20.2 km to 30.1 km (Hunt et al., 2009). The horizonal resolution is 5 km. CALIOP Level 2 Vertical Feature Mask (VFM) products provide aerosol and cloud classification along the vertical profiles, consisting of the identification of aerosols and clouds, and further the subtypes of aerosols and clouds. The layer-integrated volume depolarization ratio at 532 nm, the layer-integrated total attenuated color ratio, the layer-averaged attenuated backscatter at 532 nm, the latitude and the altitude were taken account as the inputs of the cloud-aerosol discrimination (CAD) algorithm to distinguish aerosols from clouds (Liu et al., 2019). Aerosol bins were marked as "marine", "dusty marine", "dust", "polluted dust", "continental", "polluted continental/smoke", "elevated smoke", and "others" according to the comprehensive analysis of the particulate depolarization ratio at 532 nm, the integrated attenuated backscatter coefficient at 532 nm, the layer top altitude, the layer base altitude, and the surface type (Kim et al., 2018). In this study, the

VFM products from data version 4.21 were used. The spatial resolutions of VFM products are variable: 30 m vertically and 333 m horizontally for the altitude range of -0.5 km to 8.2 km, 60 m vertically and 1000 m horizontally for 8.2 km to 20.2 km, 180 m vertically and 1667 m horizontally for 20.2 km to 30.1 km (Hunt et al., 2009).

2.3 MODIS

MODIS instrument is a Moderate Resolution Imaging Spectroradiometer, designed for the measurement of atmosphere, ocean, and land, monitoring global data with 36 high spectral resolution bands between 0.415 and 14.235 μm with spatial resolutions of 250 m (2 bands), 500 m (5 bands), and 1000 m (29 bands) (Savtchenko et al., 2004). Two MODIS instruments on board Terra satellite (10:30 equator crossing time, descending) and Aqua satellite (13:30 equator crossing time, ascending) provide near-global daily observations. In this study, we used the merged "Deep Blue/Dark Target" AOD at 550 nm ~~from~~ by averaging the daily MODIS AOD from both Terra and Aqua to get the best spatial coverage, for the purpose of smoke plume localization and Aeolus products' validation (Levy et al., 2013). The temporal resolution is daily and the spatial resolution is 1°.

2.4 VIIRS

Visible Infrared Imaging Radiometer Suite (VIIRS) onboard Suomi National Polar-Orbiting Partnership (S-NPP) satellite is a cross-track scanning radiometer with 22 spectral bands covering the visible/infrared spectrum (0.412–12.05 μm) (Liu et al., 2014). The satellite flies in a sun-synchronous polar orbit with the ascending equator crossing time of 13:30. The photo-like true-color images with the temporal resolution of daily and the spatial resolution of 250 m visualized by the Worldview (https://worldview.earthdata.nasa.gov, last access: 29 August 2025) were applied to localize the smoke plume.

2.5 MERRA-2

The Modern-Era Retrospective Analysis for Research and Applications, version 2 (MERRA-2), is the atmospheric reanalysis of the modern satellite era produced by NASA's Global Modelling and Assimilation Office (GMAO), assimilated with more than 30 types of observations including both satellite and ground-based remote sensing (Gelaro et al. 2017). The hourly column mass concentration (CMC) of organic carbon, black carbon and dust with the spatial resolution of 0.5°×0.625° from MERRA-2 were utilized to extract smoke data of ~~Aeolus~~ ALADIN observations.

2.6 HYSPLIT

The Hybrid Single-Particle Lagrangian Integrated Trajectory model (HYSPLIT) is a modelling system developed by the National Oceanic and Atmospheric Administration (NOAA) Air Resources Laboratory (ARL), which is capable to simulate the transport trajectories, dispersion and diffusion of air masses (Stein et al., 2015). In this study, both backward and forward trajectory simulations ~~with model vertical velocity~~ are applied to verify the pathway of smoke plume transport. The simulations were calculated with the model vertical velocity from the global data assimilation system developed by NOAA (https://www.ncei.noaa.gov/products/weather-climate-models/global-data-assimilation, last access: 27 March 2026).

3 Localization of the smoke ~~plume~~ transport event

In 2020, more than 8000 wildfires in the west coast of the US generated large amounts of smoke aerosol into the atmosphere continuously (https://www.fire.ca.gov/incidents/2020/, last access: 30 August 2025). A pronounced smoke transport ~~process~~ event from the western US across the Atlantic to Europe in September is presented and illustrated in Fig. 1. The daily true-color images from VIIRS and the daily mean AOD derived from Aqua and Terra are shown in this figure.

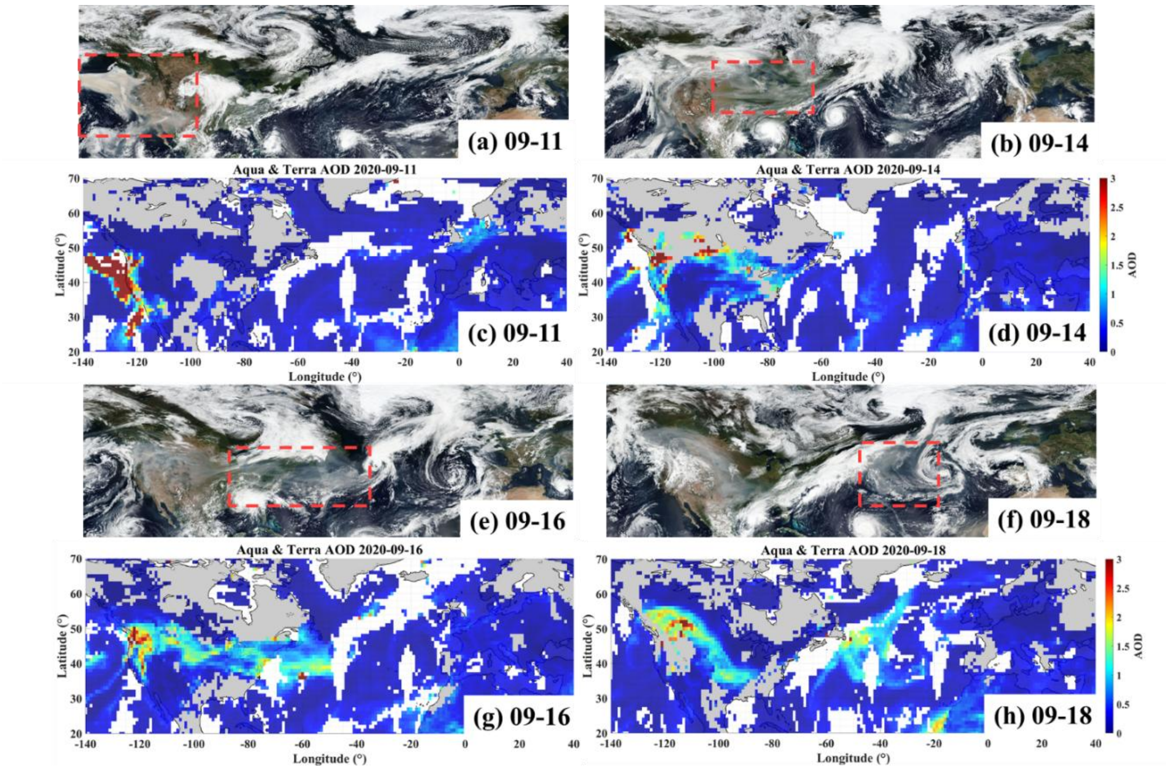

Figure 1. Observations of spaceborne passive instruments in the spatial range of 140°W to 40°E and 20°N to 70°N. True-color images from VIIRS on (a) 11, (b) 14, (e) 16, (f) 18 September 2020, acquired on the Worldview (https://worldview.earthdata.nasa.gov, last access: 29 August 2025). Averaged AOD from both Aqua and Terra on (c) 11, (d) 14, (g) 16, (h) 18 September 2020. In the AOD maps, the grey and white parts indicate the land and the invalid data, respectively.

In panel (a) of Fig. 1, the red dashed region highlights a clearly visible, dense aerosol plume over the west coast, which is likely smoke originating from wildfires in the western US.~~The daily true-color images from VIIRS and the daily mean AOD derived from Aqua and Terra are shown in this figure. The red dashed region in panel (a) highlights a clearly visible, dense smoke plume over the west coast.~~ Consistent with this observation, panel (c) indicates that many of the associated smoke layers reached AOD values greater than 3. In panels (b), (e), and (f), the visible ~~smoke~~ plumes within the red dashed boxes indicate smoke aerosols ~~plumes~~ generated off the west coast of the US and moving above the Atlantic from September 14 to 18. The maximum AOD values could exceed 1.5 during transport, as shown in panels (d), (g), and (h). Hu et al. (2022) observed smoke layers at the lidar station ATOLL (ATmospheric Observatory of LiLle) in northern France, from 17 to 22 September, which were ~~investigated~~ transported from Oregon (located on the west coast of the US) starting on 13 September. This corresponds well with the smoke plume transport indicated in Fig.1, suggesting that the smoke plume was transported to Europe afterwards. In conclusion, the snapshots taken by spaceborne passive instruments captured the daily locations of smoke plumes during their transport from the west coast of the US across the Atlantic to Europe. However, passive instruments cannot provide vertical plume information, and AOD retrieval cannot be accomplished in the presence of clouds.

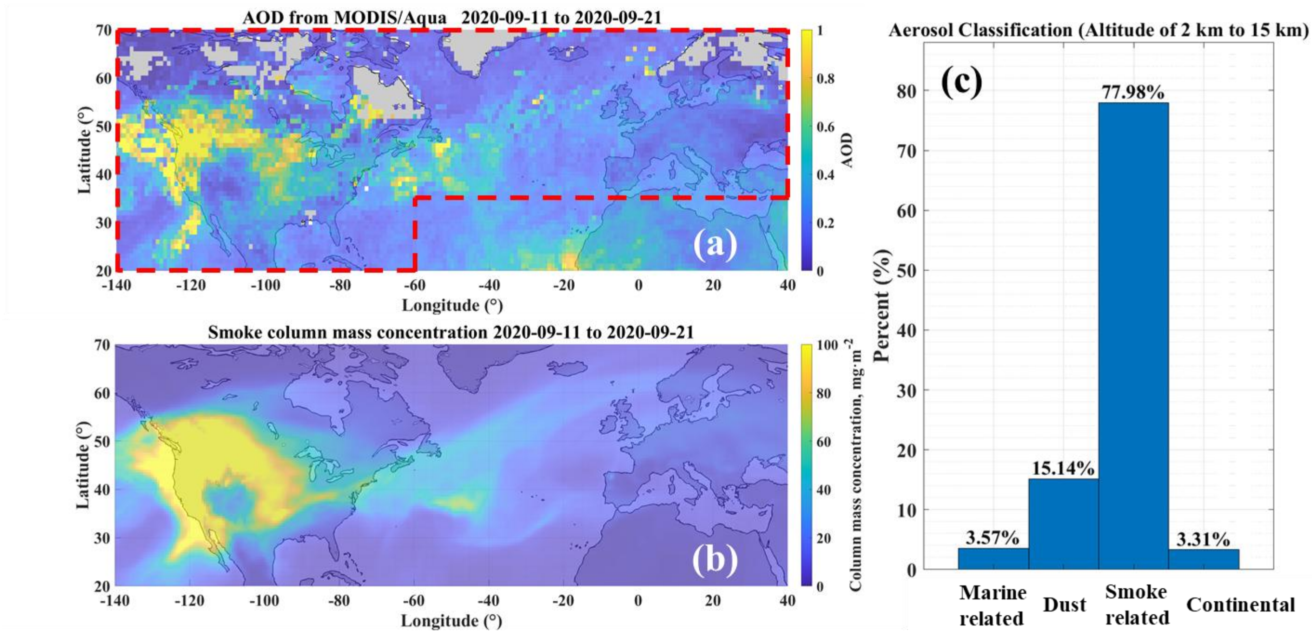

Figure 2. (a) Average AOD by MODIS onboard Aqua; (b) Average smoke column mass concentration (CMC) by MERRA-2; (c) Statistical result of aerosol classification from CALIOP VFM products, taking the data in the region indicated by the red dashed box of panel (a). The temporal range is 11 to 21 September 2020. In panel (c), "Marine related" indicates "marine" and "dusty marine" from CALIOP VFM products, and "Smoke related" includes "elevated smoke", "polluted continental/smoke", "polluted dust".

In order to further investigate the pathway of the ~~enitre~~entire smoke transport ~~process~~event, the averaged AOD and the smoke CMC with the same spatial coverage and the temporal range from 11 to 21 September 2020 are presented individually in panels (a) and (b) of Fig. 2. The smoke CMC was calculated as the sum of the organic carbon and black carbon from the MERRA-2 reanalysis dataset. In general, these two figures align well for regions with high values, except for the Sahara Desert and the surrounding ocean, which have high load of atmospheric dust. From ~~there~~ these figures, the transport pathway is visible. The smoke plume moved eastward from the west coast of the US, crossing the continental US and reaching the central Atlantic. Then, it separated into two branches. The larger branch moved northeastward over a longer distance, while the smaller one moved southeastward. The southern smoke plume was transported toward the Sahara Desert, where it may have mixed with dust aerosols. Overall, the gradual decrease in AOD and smoke CMC from west to east suggests that the concentration of the smoke aerosol diminished due to diffusion during its transport. However, it can be speculated that the accumulation of smoke plumes occurred over the Atlantic between longitude 70°W and 40°W after being transported away from land, as the AOD and the smoke CMC show higher values than the surrounding region. As previously mentioned, the Aeolus's ALADIN lidar cannot classify aerosol subtypes due to the lack of ~~δ~~ depolarization ratio detection (Flament et al., 2021). Whether ALADIN can characterize the smoke plumes during transport depends on interference from other types of aerosols along the transport pathway. Therefore, an examination of the types of aerosols in the smoke pathway region was conducted. Data from the CALIOP VFM product was used. The aerosol subtype data within the altitude of 2 km to 15 km and the period of 11 to 21 September, located in the red dashed box of Fig.2 (a), was counted for the statistical analysis. The result shown in Fig. 2 (c) indicates that the smoke-related aerosols (flagged as "elevated smoke", "polluted continental/smoke", "polluted dust" in the VFM product) dominate the region, accounting for around 78% of the total. Dust aerosol accounts for around 15%, while the sum of the others (marine-related and continental) accounts for less than 7%.

~~To conclude, in this section~~In summary of this section, ~~we captured daily "snapshots" of the smoke plume during its transport from the west coast of the US across the Atlantic to the Europe. Furthermore,~~ the specific period and pathway of the smoke transport were ~~verified~~ identified and the transport region was found dominated by the smoke-related aerosols. The results indicate the potential for deriving smoke properties from Aeolus L2A products for this smoke event, as the transport exhibited a large spatial and temporal scale with limited influence from other aerosol types.

4 Development and validation of the Aeolus-based smoke dataset

In this section, focusing on the smoke transport event described in Section 3, the procedures for developing an Aeolus-based smoke dataset are presented in Sections 4.1 and 4.2. Aeolus L2A products within the spatial domain of 140°W–40°E and 20°N–70°N during the period from 11 to 21 September 2020 were utilized, covering the entire transport event. The caveats and uncertainties are analysed in Section 4.3. The validation of this dataset is presented in Section 4.4. The brief flowchart of the methodology introduced in this section is summarized in Figure 3.

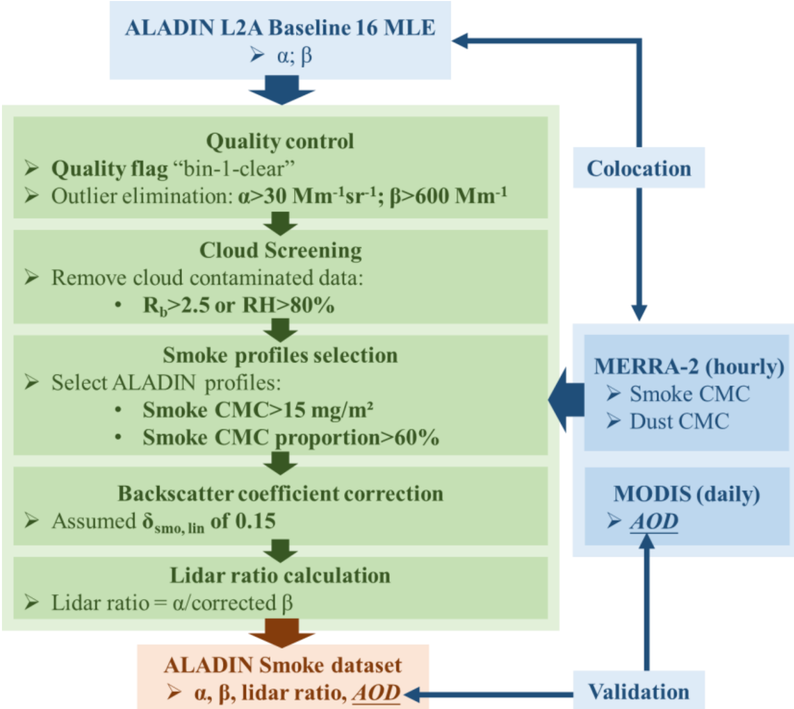

Figure 3. Methodology flowchart for development and validation of the Aeolus-based smoke dataset. α and β represent ALADIN observed extinction and backscatter coefficients. R_b and RH represent backscattering ratio and relative humidity. CMC is column mass concentration and $\delta_{smo,\,lin}$ is smoke linear depolarization ratio.

4.1 Collocation of multi-platform data

The smoke CMC data from MERRA-2 and ~~The~~ the AOD data from MODIS ~~and the smoke CMC data from MERRA-2~~ are used for deriving and validating the Aeolus-based smoke dataset, respectively. Daily AOD averages are based on data from MODIS onboard Terra and Aqua. Due to the different spatial resolutions, these data were collocated to the Aeolus data grid, which follows the Aeolus orbit. The AOD data from MODIS used in this study is with a spatial resolution of 1° and a temporal resolution of one day. The smoke CMC data from MERRA-2 has a spatial resolution of 0.5°×0.625° and a temporal resolution of one hour. For the collocation, the temporal closest and spatial nearest data bins of AOD and smoke CMC to the Aeolus data grid, which has a horizontal resolution of 90 km along its orbits were selected. However, the time difference between Aeolus and ~~MODIS~~ Terra or Aqua can be several hours, while the difference between Aeolus and MERRA-2 can be tens of minutes, due to their distinct temporal resolutions.

4.2 Derivation of the smoke dataset from ~~Aeolus~~ ALADIN observations

The extinction and backscatter coefficients measured by Aeolus contain information ~~of~~ on both clouds and aerosols. In order to characterize the features and the evolution of the smoke plumes during transport, a smoke dataset including extinction coefficient, backscatter coefficient and lidar ratio from Aeolus observations products should be acquired. Therefore, several steps were adopted to derive smoke data from the Aeolus L2A products:

(1) Bins selectionQuality control. The flag “bin-1-clear” (set to 1), indicating normally detected profiles, inside the Aeolus L2A product was used for the preliminary quality control. Thresholds were set for the outlier elimination of backscatter and extinction coefficients. Backscatter coefficients larger than 30 $Mm^{-1}sr^{-1}$ and extinction coefficients larger than 600 Mm^{-1} were eliminated.

(2) Cloud screening. We applied a similar method to that used in the marine aerosol research of Sun et al. (2024). Data bins with a backscatter ratio (R_b, calculated by dividing the total backscatter coefficient by the molecular backscatter calculated by total backscatter coefficient dividing molecular backscatter coefficient) higher than 2.5 are identified as cloud contamination. The threshold of relative humidity (RH) was set more strictly than in Sun et al. (2024), such that clouds are considered to exist with a high possibility when RH is above 80% (Forbes et al., 2009). Consequently, Aeolus L2A data bins with R_b and RH no more than 2.5 and 80% are considered as aerosol data bins.

(3) Smoke profiles selection. The Aeolus aerosol dataset from Aeolus L2A has been acquired by step 1 and 2. As introduced in Section 3, CALIOP classified about 15% of the aerosols in the smoke transport region were as dust. CMC data from MERRA-2 was utilized to select the L2A profiles with smoke aerosols. A Level 2A profile can be considered a “smoke profile” if it meets the following two criteria: a smoke CMC greater than 15 mg/m² and a smoke CMC proportion (calculated by the smoke CMC dividing the sum of the smoke CMC and the dust CMC) exceeding 60%.

(4) Backscatter coefficient correction. Due toSince Aeolus ALADIN missed missing the cross-polar component of the particle backscattered signals, the lidar original backscatter coefficients from Aeolus L2A products wereratio calculated directly by the original extinction and backscatter was overestimatedunderestimated. Thus, the correction is supposed to be performedneeded in order to obtain the total backscatter coefficient. Additionally, as ALADIN was a circular polarization lidar system, the smoke circular depolarization ratio ($\delta_{\mathrm{smo,\ cir}}$) converted from $\delta_{\mathrm{smo,\ lin}}$ should be used for the correction. The backscatter correction was accomplished applying the formulas below (Roy and Roy, 2008; Paschou et al., 2022):

$$\delta_{\mathrm{smo,cir}} = \frac{2\delta_{\mathrm{smo,lin}}}{1-\delta_{\mathrm{smo,lin}}} \tag{1}$$

$$\beta_{smo} = (1+\delta_{\mathrm{smo,cir}})\beta_{Aeolus} \tag{2}$$

In terms of this smoke transport event, it has been investigated determined that the $\delta_{\mathrm{smo,\ lin}}$ at 532 nm over the continental US is about 0.1 and the $\delta_{\mathrm{smo,\ lin}}$ at 355 nm over the Europe is around 0.15 (Hu et al., 2022). We also investigated theThe stability of $\delta_{\mathrm{smo,\ lin}}$ during long transport, as well as the impact of their variation on total backscatter coefficient and lidar ratio in the followingshould be discussed. Using the L2 APro product and L2 VFM product of CALIOP from 11 to 21 September, we examined the variation of $\delta_{\mathrm{smo,\ lin}}$ in the smoke transport pathway. The particulate linear depolarization ratio data bins in the L2 APro product identified as the smoke-related aerosols (flagged as “elevated smoke”, “polluted continental/smoke”, “polluted dust” in the VFM product) were utilized for analysis. Since the transport was generally eastward, the red box region in panel (a) of Fig. 2 was divided into 9 sub-regions, each 20° wide zonally from 140°W to 40°E. The average $\delta_{\mathrm{smo,\ lin}}$ values were calculated for these sub-regions and presented in Table 1. The highest value, 0.119, appeared in the subregion between 100°W and 80°W, while the lowest value, 0.110, appeared in the subregion between 20°W and 20°E. Basically, the average $\delta_{smo, lin}$ at 532 nm exhibits a slight decline trend from west to east during smoke transport. ~~This variation is presented in Table A1 in the appendix.~~ Additionally, the $\delta_{smo, lin}$ at 355 nm of 0.16 and the $\delta_{smo, lin}$ at 532 nm of 0.12 were observed by Hu et al. (2022) for the same smoke transport event, from which we can derive that $\delta_{smo, lin}$ at 355 nm is approximately 1.33 times that at 532 nm. Using a mean value of 0.115 from Table 1, this crude approximation yields that $\delta_{smo, lin}$ at 355 nm is approximately 0.15. Therefore, we set the assumed $\delta_{smo, lin}$~~linear depolarization ratio ($\delta_{assu, lin}$)~~ at 355 nm to 0.15 for the entire transport, ~~process, slightly higher than the CALIOP measurements at 532 nm, to be in line with the observation of Hu et al. (2022) at 355 nm, but don't~~considering no anticipated significant zonal variability ~~as~~ indicated by the CALIOP observations at 532 nm. ~~Assuming a smoke bin with an extinction coefficient (α_{smo}) of 202.5 Mm^{-1} and a Aeolus measured backscatter coefficient (β_{Aeolus}) of 3 $Mm^{-1}sr^{-1}$, with a $\delta_{assu, lin}$ of 0.15 (a assumed circular depolarization ratio ($\delta_{assu, cir}$) of 0.35), the measured total smoke backscatter coefficient (β_{meas}) can be calculated as 4.05 $Mm^{-1}sr^{-1}$, then the measured lidar ratio (L_{meas}) is 50 sr (a typical smoke lidar ratio at 355 nm). However, if there is a $\delta_{assu, lin}$ bias of 0.01 with the real linear depolarization ratio ($\delta_{real, lin}$) of 0.14 (the real circular depolarization ratio ($\delta_{real, cir}$) of 0.33), the real total smoke backscatter (β_{real}) can be calculated as 4 $Mm^{-1}sr^{-1}$ and the real lidar ratio (L_{real}) is 50.6 sr. In contrast, if the $\delta_{real, lin}$ is 0.16 ($\delta_{real, cir}$ is 0.38),β_{real} is 4.14 $Mm^{-1}sr^{-1}$ while L_{real} is 48.9 sr. Therefore, it can be summarized that, under these circumstances, if $\delta_{real, lin}$ varies from 0.14 to 0.16, then β_{real} will be within the range of 4 $Mm^{-1}sr^{-1}$ to 4.14 $Mm^{-1}sr^{-1}$ and L_{real} will be within the range of 48.9 sr to 50.6 sr. Namely, the L_{real} is around 50±1 sr when the $\delta_{real, lin}$ is 0.15±0.01. Assuming that the L_{meas} maintains a value of 50 sr and that the $\delta_{real, lin}$ declines by around 0.01 from 0.15 to 0.14 (assuming the same variation at 355 nm as at 532 nm throughout the entire transport), the constant $\delta_{assu, lin}$ at 355 nm of 0.15 could lead to an underestimation of the L_{meas} by the maximum error of around 1 sr. As shown in Table A1, the standard deviation of $\delta_{smoke, lin}$ at 532 nm can vary for an individual sub-region, with an approximate value of 0.085. Nevertheless, the corrected Aeolus β_{meas} and L_{meas} values are only used for the statistical analyses of a single measurement cross-section or a specific sub-region. Therefore, the effect of the assumed constant $\delta_{assu, lin}$ on β_{meas} and L_{meas} is considered negligible after averaging within each cross-section or sub-region.~~

Table 1. Depolarization ratio (mean ± standard deviation) at 532 nm of the smoke plume and the corresponding data bin counts during transport from 140°W to 40°E, derived from CALIOP observations.

Longitude ranges of Sub-regions	140°W-120°W	120°W-100°W	100°W-80°W	80°W-60°W	60°W-40°W	40°W-20°W	20°W-0°	0°-20°~~W~~E	20°E-40°~~W~~E
Depolarization ratio (mean±std)	0.119 ±0.087	0.117 ±0.088	0.119 ±0.088	0.114 ±0.088	0.116 ±0.087	0.111 ±0.083	0.110 ±0.083	0.110 ±0.085	0.116 ±0.086
Data bin counts	105624	212699	131722	112280	80926	80484	86948	135184	149671

~~**Table A1. Depolarization ratio at 532 nm of the smoke plume during transport from 140°to 40°E, derived from CALIOP observations.**~~

(5) Lidar ratio calculation. Smoke lidar ratios were calculated for each data bin of smoke profiles by dividing extinction coefficients by the corrected backscatter coefficients.

One cross-section example that was processed using the five steps above and the corresponding orbit is shown in Fig. ~~3~~4. ~~This figure~~Panel (a) shows aerosol extinction coefficients of Aeolus crossing the smoke plume on 15 September 2020. The cross-section started at 11:51:59 (UTC) on 70.0° N, 75.8°W and ended at 12:04:47 (UTC) on 20.5°N, 91.1°W, crossing the eastern US on a descending orbit. The black bins indicate the invalid values while the gray ones indicate the cloud contaminated bins. They were all removed for subsequent characterization. Within the red dashed lines, the "smoke profiles" captured a thick smoke layer alongside a cloud layer. The maximum altitude was around ~~12~~ 10 km, and the latitude range was 33°N to 48°N (with a meridional width of more than 1500 km).

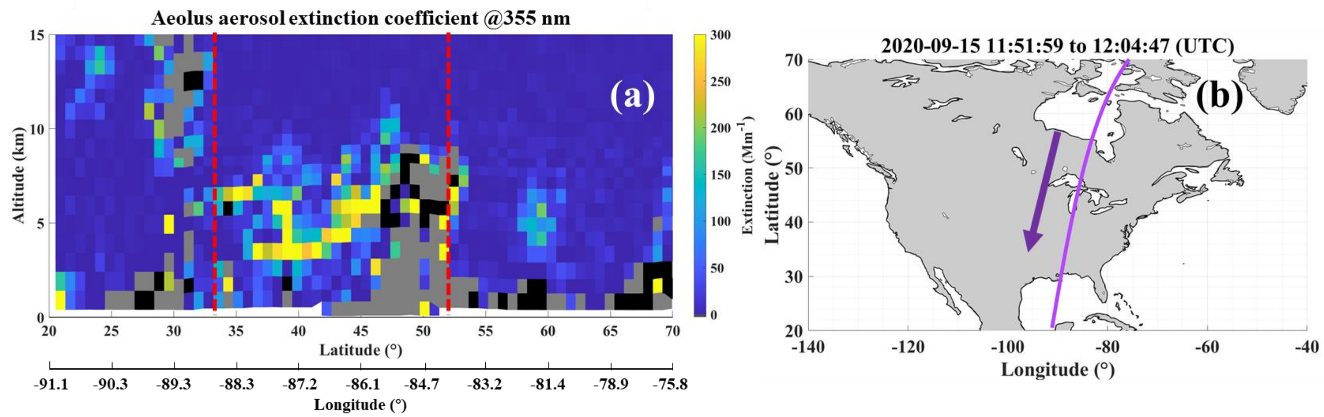

Figure ~~3~~4. (a) One cross-section example of Aeolus aerosol extinction coefficient crossing the smoke plume, on 15 September 2020, starting at 11:51:59 (UTC) on 70.0°N, 75.8°W and ending at 12:04:47 (UTC) on 20.5°N, 91.1°W. (b) The corresponding descending orbit ~~is presented in Fig. 5 (b)~~indicated by the purple curve (Aeolus orbit) and the purple arrow (Aeolus flight direction). The data in panel (a) has been processed to derive smoke data from Aeolus by the steps introduced in the section "Derivation of the smoke dataset from ~~Aeolus~~ ALADIN observations". The black bins indicate the invalid values, while the grey ones indicate the cloud contaminated bins. The profiles inside two red dashed lines are the "smoke profiles".

4.3 Caveats and uncertainties

This section outlines the caveats and potential uncertainties associated with the five steps used to derive the smoke dataset, as introduced in Section 4.2. Steps (1) through (3) are limited to data bin selection and thus do not introduce uncertainties beyond those inherent in the Aeolus observational data. Step (4), "backscatter correction," adopts an assumed depolarization ratio for both backscatter coefficient and lidar ratio correction. This step could introduce additional uncertainties, which will be discussed in detail below.

In step (1), "quality control," preliminary quality control was conducted using the Aeolus flag and outlier elimination based on thresholds. The principle for threshold setting is that values exceeding than the thresholds are unlikely to originate from typical aerosol cases; they could represent outliers or be contaminated by clouds. After processing the selected Aeolus data (spatial domain: 140°W-40°E, 20°N-70°N; period: 11-21 September 2020) by step (1), 95% of extinction coefficients (174819 out of 183997 data bins) and 95% of backscatter coefficients (175002 out of 183997 data bins) were retained as valid data bins. Step (2), "cloud screening," applies thresholds of R_b and RH, as cloud layers are characterized by stronger backscattering and higher RH. After step (2), 87% of extinction coefficients (151922 out of 174819 data bins) and 86% of backscatter coefficients (150210 out of 175002 data bins) were retained as aerosol data bins. The risk here is that even a few weak clouds with particularly low R_b and RH could contaminate the smoke dataset. In step (3), "smoke profiles selection," hourly data from the MERRA-2 reanalysis dataset are used. The time gaps between colocated Aeolus and MERRA-2 data are less than one hour, during which the smoke layers are considered stable. Thus, the "smoke profiles" can be selected with the assistance of MERRA-2 dataset. After applying the smoke proportion threshold of 60%, a mean smoke proportion of 79% was computed from the selected smoke profiles. This indicates that the smoke dataset may contain a small amount of dust aerosol contamination.

With respect to step (4), the assumption of a constant linear depolarization ratio for backscatter coefficient and lidar ratio correction was based on the observations reported by Hu et al. (2022) and corresponding CALIOP measurements. It should be noted that this constant may vary depending on the characteristics of distinct smoke events. The assumption could introduce additional uncertainties. Regarding the calculation of uncertainties in the total backscatter coefficient and lidar ratio resulting from the depolarization ratio correction, the relevant formulas can be derived using equations (1) and (2), as shown below:

$$\sigma_{\beta_{smo}} = \frac{2\beta_{Aeolus}}{1-\delta_{smo,lin}} \cdot \sigma_{\delta_{smo,lin}} \qquad (3)$$

$$\sigma_{L_{smo}} = \frac{2\frac{\alpha_{Aeolus}}{\beta_{Aeolus}}}{(1+\delta_{smo,lin})^2} \cdot \sigma_{\delta_{smo,lin}} \qquad (4)$$

Among them, α_{Aeolus} and β_{Aeolus} are the extinction and backscatter coefficients observed by Aeolus, while $\delta_{smo,lin}$ and $\sigma_{\delta_{smo,lin}}$ represent the smoke linear depolarization ratio and its corresponding uncertainty, respectively. Using these two formulas, the uncertainties of the total backscatter coefficient ($\sigma_{\beta_{smo}}$) and the lidar ratio ($\sigma_{L_{smo}}$) can be obtained.

Utilizing these formulas, the uncertainties within a single smoke layer captured by one Aeolus cross-section as well as those across different transport stages, will be discussed as follows. First, to investigate the uncertainties introduced by depolarization ratio, assuming α_{Aeolus} of 200 Mm^{-1} and β_{Aeolus} of 3 $Mm^{-1}sr^{-1}$ as constants, under both circumstances. $\delta_{smo,lin}$ is set to the assuming constant of 0.15. For the uncertainty within a single cross-section, $\sigma_{\delta_{smo,lin}}$ of 0.085 is adopted, derived from the standard deviations of sub-regions presented in Table 1. Applying formulas (3) and (4), $\sigma_{\beta_{smo}}$ and $\sigma_{L_{smo}}$ are computed as 0.6 $Mm^{-1}sr^{-1}$ and 8.6 sr, respectively. Although this estimation is contingent upon specific assumptions and the use of CALIOP-derived $\sigma_{\delta_{smo,lin}}$, this approximate uncertainty quantification demonstrates that $\sigma_{\beta_{smo}}$ and $\sigma_{L_{smo}}$ per data bins attributable to $\sigma_{\delta_{smo,lin}}$ may exceed the uncertainties within a single cross-section (as indicated by the standard errors of the mean listed in Table 1). It should be illustrated that the standard errors of the mean in Table 2 do not incorporate the uncertainty estimation described above, as no accurate depolarization information was available for the Aeolus observations. As for the uncertainties introduced by depolarization ratio across different transport stages, the $\sigma_{\delta_{smo,lin}}$ is set to 0.009, which is the largest deviation from the mean depolarization ratio values presented in Table 1. This procedure tests whether the longitudinal changes in the backscatter coefficient and lidar ratio discussed in Section 5 remain robust when the variation in the linear depolarization ratio is considered. Under this assumption, $\sigma_{\beta_{smo}}$ and $\sigma_{L_{smo}}$ can be calculated as 0.06 Mm^{-1}sr^{-1} and 0.9 sr, respectively, using formulas (3) and (4). Considering the mean lidar ratio values of the different cross-sections shown in Table 2, the maximum variation is around 20 sr. Therefore, under the assumption that $\delta_{smo,lin}$ is 0.15, $\sigma_{\beta_{smo}}$ and $\sigma_{L_{smo}}$ are negligible and will not affect the trends of the mean values across different longitudinal transport stages. In conclusion, while correcting the smoke backscatter coefficient and lidar ratio using $\delta_{smo,lin}$ of 0.15 may introduce additional uncertainties for each data bin (0.6 Mm^{-1}sr^{-1} for backscatter coefficient and 8.6 sr for lidar ratio), the corrected results are used for only the mean value analyses of a single measurement cross-section or a specific sub-region in the following discussion.

4.4~~3~~ Validation of the Aeolus smoke dataset

The performance of ALADIN aerosol profiles has been examined and demonstrated in several validation studies, including Baars et al. (2021), Abril-Gago et al. (2022), Gkikas et al. (2023), and Trapon et al. (2025). Among these, Baars et al. (2021) conducted co-temporal profile comparisons between ALADIN and a ground-based lidar and confirmed ALADIN's capability for profiling backscatter coefficient, extinction coefficient, and lidar ratio within a smoke layer. This smoke layer was transported from the US, and its transport closely matches and slightly precedes the transport event examined in the present study. Nevertheless, for the purpose of verifying the reliability of the derived Aeolus smoke dataset across the entire transport, spaceborne measurement provide data with much larger spatial coverage compared to ground-based lidars, which are limited to specific stations. For a transatlantic dust transport event in June 2020, ALADIN aerosol observations were compared with CALIOP, despite a temporal gap of several hours and a limited number of well-matched orbits (Song et al., 2024). Considering the scarcity of well-matched orbits, the lack of a cross-polar component in ALADIN backscatter coefficient measurements, and the reliance of CALIOP extinction coefficient retrieval on assumed lidar ratios, we decided to use MODIS for AOD validation. Despite the temporal gap of several hours between ALADIN and MODIS, the averaging of Terra and Aqua MODIS data, together with the statistical results based on a large number of data points (N = 1247, as shown in Figure 5), can provide evidence for ALADIN validation to some extent. ~~For the purpose of verify the reliability of the derived Aeolus smoke dataset, collocated AOD from MODIS was used for validation.~~

The ~~validation~~ dataset covers the period from 11 to 21 September 2020, and the spatial range is from 140°W to 40°E and 20°N to 70°N. ~~In consideration of~~Considering that ALADIN (355 nm) and MODIS (550 nm) AOD are in different wavelength and only smoke AOD is compared, the wavelength conversion was conducted. The Ångström exponent of 0.2~~2~~5 was applied to the conversion from 34~~40~~55 nm to 50~~00~~32 nm (ÅE$_{3}$$_{55}$~~$_{40-5}$~~$_{32}$~~$_{00}$~~), as reported by Hu et al. (2022) for the same smoke event. The low ÅE$_{355-532}$~~ÅE$_{340-500}$~~ suggests that the smoke plumes could be dominated by the coarse mode aerosols. We also consider it acceptable to use ÅE$_{355-532}$~~ÅE$_{340-500}$~~ for a similar wavelength range (355 nm to 550 nm), assuming the Ångström exponent is constant within the range of ~~340~~355 nm to 550 nm. The conversion was accomplished using the following formula:

$$AOD_{550\,nm} = AOD_{355nm}\exp(ÅE_{35540-53200}\,ln\frac{355}{550}) \quad (5)$$

Basically, the scatter between the MODIS AOD at 550 nm and the ALADIN AOD both at 355 550 nm is , presented in Fig. 4 5 (a), indicatinges a reasonable degree of agreement, given their distinct measurement techniques, different spatial grids and overpass times. However, when focusing on the AOD range of 0 to 0.5, it can be determined that the ALADIN AODs are larger than the MODIS AODs, as more yellow bins indicating higher counts appear above the red dashed line presenting the "y=x". In addition, iIt is evident that the ALADIN AODs are generally less than 2 1.5 when the MODIS AODs range from 2 1.5 to 3, illustrating that the MODIS AODs are higher thanexceed ALADIN AODS when the AODs areunder relatively high AOD conditions. To investigate more specifically, based on the abovethese features, we separated the AODs into two groups based on AODaccording to their deviation (ALADIN minus MODIS)values. -The low AOD group consists of AOD values below 1, while The the high AOD group comprises either ALADIN or MODIS AOD values above 1consists of ALADIN AOD or MODIS AOD values larger than 1, while the low AOD group consists of AOD values smaller than 1. The AOD deviations between the ALADIN (355 nm) and MODIS (550 nm) measurements for the high low and low high AOD groups are presented in the histograms of in panel (b) and panel (c) in Fig. 45 (b) and Fig. 5 (c). With respect to the low AOD group, the number of matched pairs (N) is 916 while mean bias (BIAS) is -0.024 and mean absolute error (MAE) is 0.19. These results indicate good agreement and suggest that, compared with MODIS, the Aeolus smoke dataset can provide reliable AOD and extinction coefficient when AOD is below 1. -For the high AOD group, the count number (N) of the matched pairs is 331, with a mean bias (BIAS) of -0.4259 and a mean absolute errorMAE of 0.721. It has been reported that, during severe smoke events, MODIS AOD (derived using with either the Deep Blue or Dark Target algorithm) could may overestimate the AOD under high AOD conditionswhen it is high (Gumber et al., 2023). With respect to the low AOD group, N is 916 while BIAS is 0.058 and MAE is 0.22. The slight positive BIAS illustrates that the ALADIN AOD at 355 nm is larger than the MODIS AOD at 550 nm. This result is consistent with the Ångström power law (Ångström, 1964). This finding could explain the overestimation of MODIS AOD observed in this study. In consideration of only smoke AOD is compared, the wavelength conversion was conducted. The Ångström exponent of 0.2 was applied to the conversion from 340 nm to 500 nm ($ÅE_{340-500}$), as reported by Hu et al. (2022) for the same smoke event. The low $ÅE_{340-500}$ suggests that the smoke plumes could be dominated by the coarse mode aerosols. We also consider it acceptable to use $AE_{340-500}$ for a similar wavelength range (355 nm to 550 nm), assuming the Ångström exponent is constant within the range of 340 nm to 550 nm. The conversion was accomplished using the following formula:

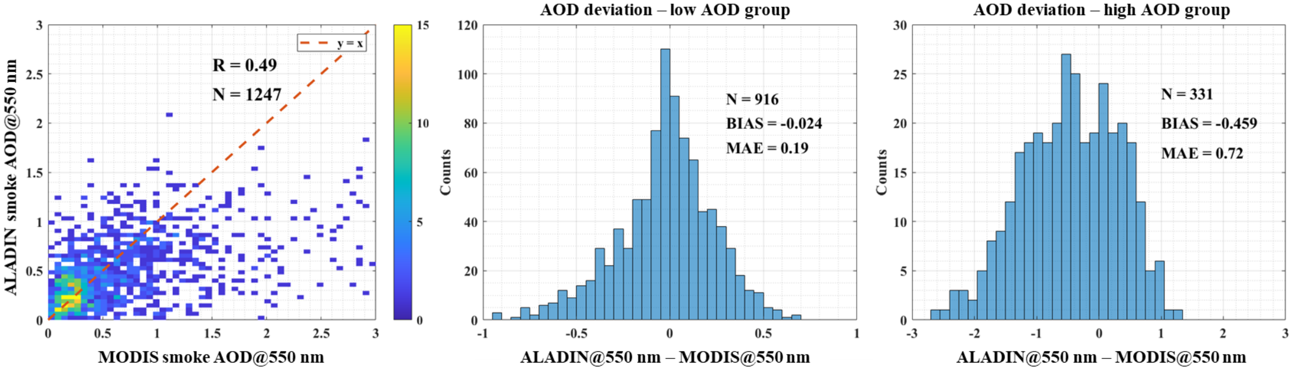

Figure 45. Comparison results between converted ALADIN AOD and MODIS AOD, both at 550 nm. (a) Scatter of MODIS AOD at 550 nm and ALADIN AOD at 355 nm. AOD deviation histograms of ALADIN AOD at 355 nm minus MODIS AOD at 550 nm for (b) high AOD group and (c) low AOD group. (d) AOD deviation histograms of converted ALADIN AOD at 550 nm minus MODIS AOD at 550 nm for low AOD group.

$$AOD_{550\ nm} = AOD_{355nm} \exp\left(ÅE_{340-500}\, ln \frac{355}{550}\right) \quad (2)$$

The AOD deviation between the converted ALADIN and MODIS AOD both at 550 nm is shown as the histogram in Fig. 4 (d). The BIAS presents evident reduction to 0.02, while the MAE slightly decreased to 0.2. These results indicate better agreement and indicates that the AOD and extinction in the Aeolus smoke dataset are reliable.

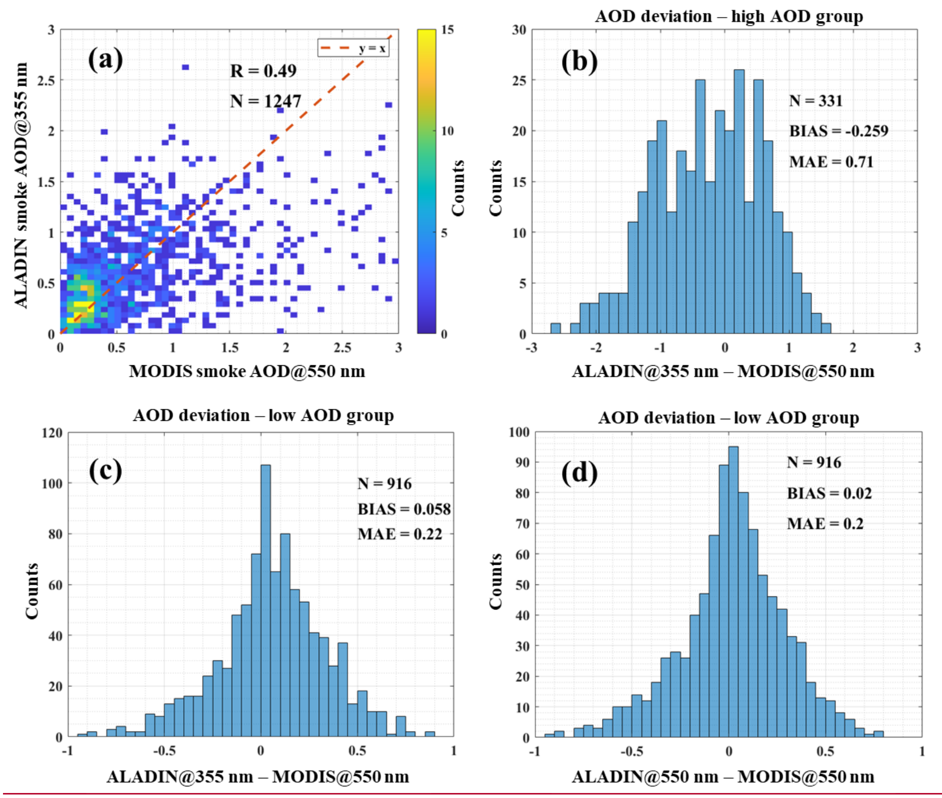

5 Characterization of the smoke aerosols~~of the smoke~~ across the transport

5.1 Cross-sections of the smoke aerosol layers~~Cross-sections~~ ~~representing~~ at different transport ~~phases~~stages

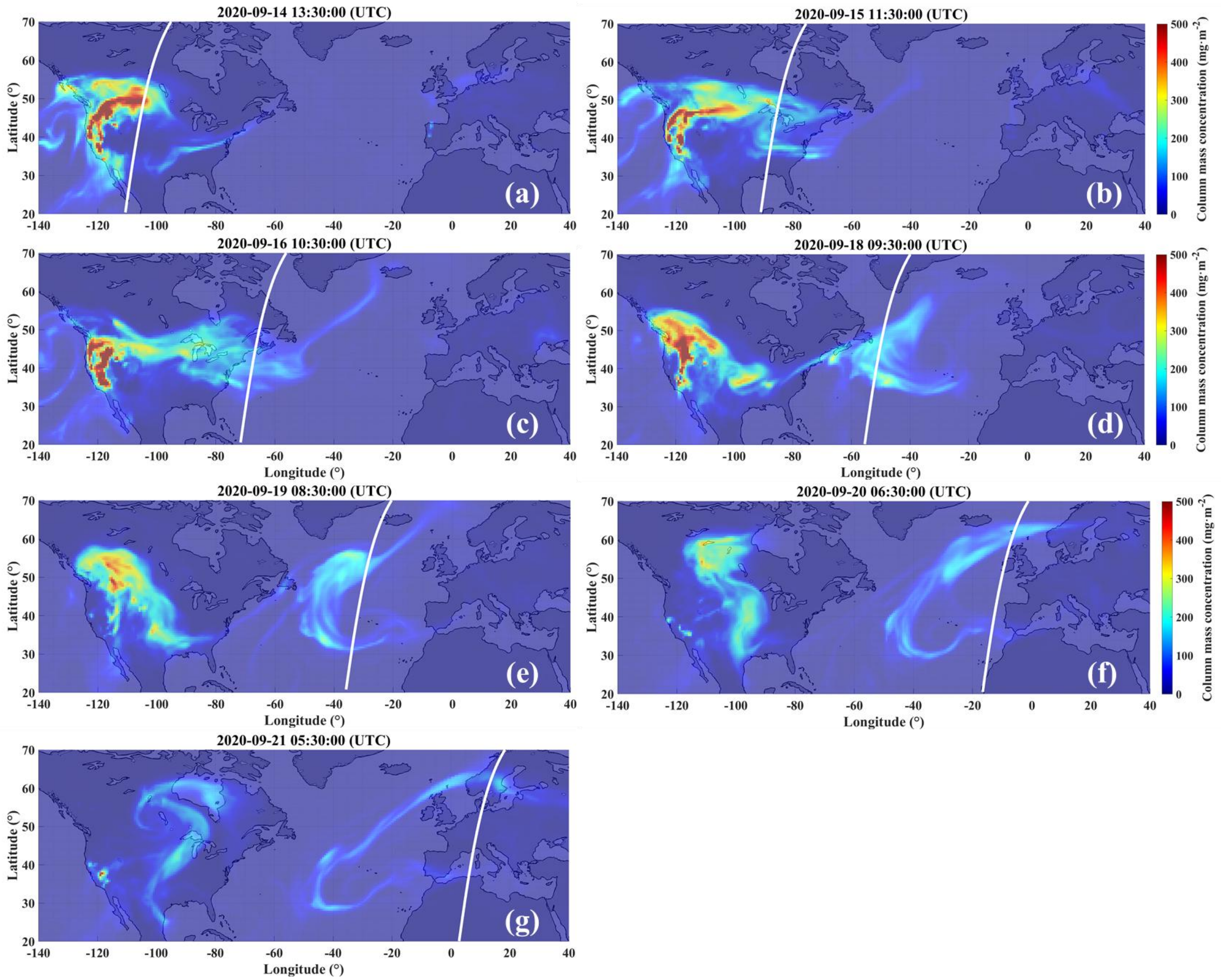

Figure ~~5~~6. Smoke column mass concentration map in the spatial range of 140°W to 40°E, 20°N to 70°N, on (a) 14, (b) 15, (c) 16, (d) 18, (e) 19, (f) 20, (g) 21 September 2020, respectively. The white curves indicate the selected Aeolus orbits on the same days.

Seven ~~Aeolus~~ ALADIN observations with descending orbits from west to east, from 14 to 21 September were selected, intended for analysing the smoke layers at ~~the representing~~ different transport ~~phases~~ stages~~of the smoke transport process~~. The locations of these cross-sections are shown as the white curves in Fig. ~~5~~6, with the background smoke CMC maps temporally closest to every Aeolus orbit. From the smoke CMC maps, it can be clearly seen that a smoke plume generated from the west coast of the US, crossing the continental US and reached the Atlantic. There, it likely separated into two plumes. One of them, the larger one, arrived in Europe, while the other propagated ~~came~~ to the Mediterranean. The seven Aeolus orbits, all of which cross the smoke plumes indicated by the smoke CMC maps, have the potential to capture cross-sections of the smoke plumes ~~in~~ at different transport ~~phases~~stages.

5.1.1 General transport pathway analysis by the cross-sections

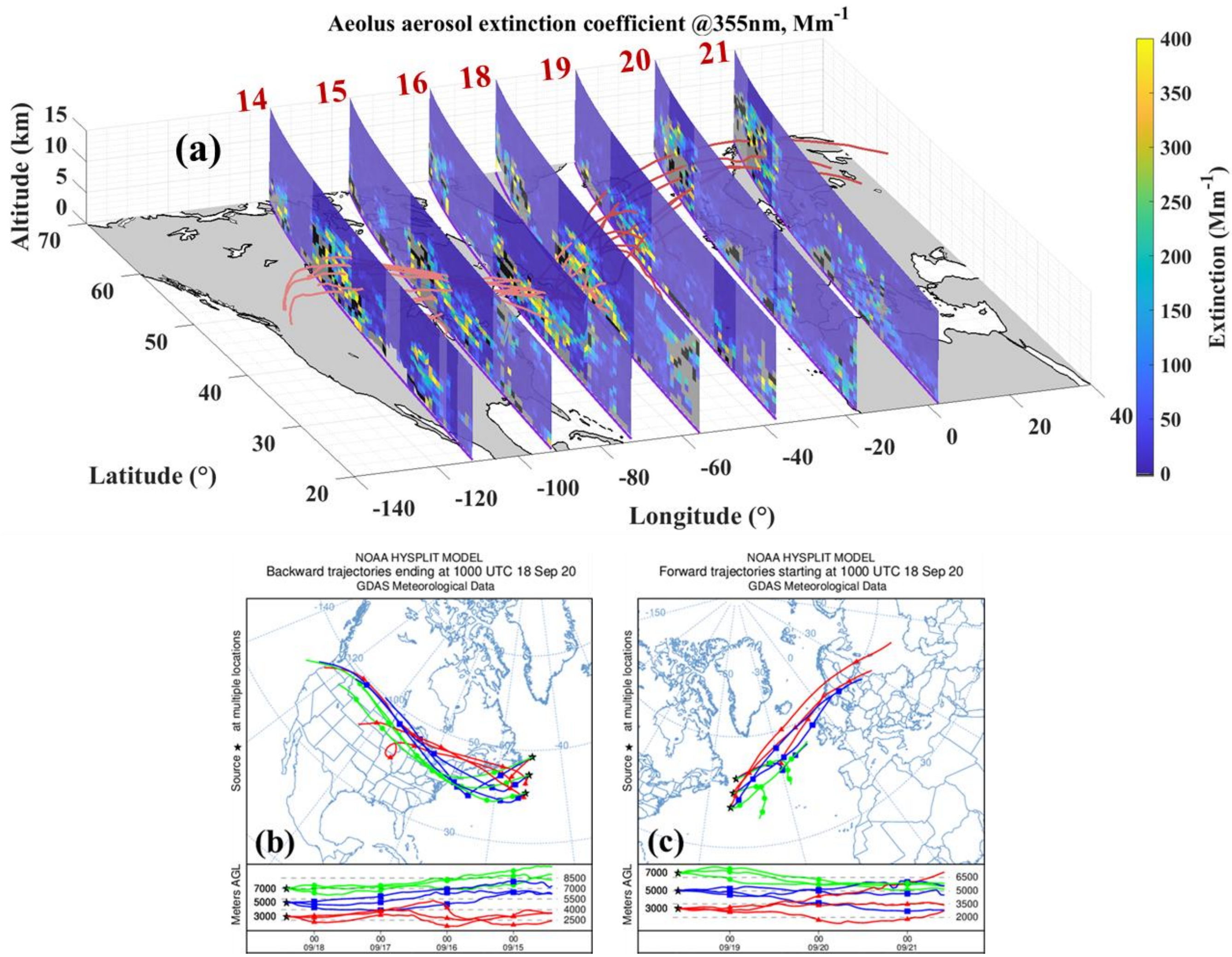

Figure ~~6~~7. (a) The selected cross-sections of Aeolus aerosol extinction coefficient at 355 nm on 14, 15, 16, 18, 19, 20, 21 September 2020, with the HYSPLIT trajectories starting from 18 September. In the cross-sections, the black and grey bins indicate invalid data and cloud contaminated data separately, while the pink curves present the backward trajectories and the red curves are the forward trajectories. The dark parts of the curtains indicate smoke profiles identified by the step (3) in Section 4.2. Details of the (b) backward and (c) forward trajectories originating from the middle of the transport pathway (acquired by https://www.ready.noaa.gov/HYSPLIT_traj.php, last access: 7 September 2025).

Figure ~~6~~7 (a) shows the seven selected cross-sections of the Aeolus aerosol extinction coefficient at 355 nm from September 14 to 21. The black bins indicate invalid data, and the white bins indicate cloud-contaminated data. The dark regions are considered to consist of "smoke profiles," but the bright regions did not meet the criteria introduced in Section 4.2 and were therefore not considered for further analysis. The backward and forward trajectories are also plotted in Fig. ~~6~~ 7 (a), indicated by pink and red curves, respectively. The details of the trajectories are shown in Fig 6 (b) and (c). The starting time is 10:00

UTC on 18 September 2020 and the starting locations were determined by the smoke layers in the Aeolus cross-section on that day. The locations are 49.49°W, 48.55°N; 50.52°W, 44.62°N; and 51.44°W, 40.69°N. They are all in the smoke layers at altitudes of 3000 m, 5000 m, and 7000 m. The duration of the backward trajectories is 96 hours ending at 10:00 UTC on 14 September, while the duration of the forward trajectories is 72 hours ending at 10:00 UTC on 21 September. ~~The~~ All seven cross-sections captured the smoke layers, and these layers show good agreement with the HYSPLIT trajectories. Considering that the seven Aeolus orbits crossed the smoke plumes indicated by the CMC maps (as presented in Fig. 6), it can be inferred from the above facts that the smoke layers observed in the seven cross-sections originated from the same smoke plume but at different transport stages.~~cross-sections capturing the smoke layers and the trajectories match well with each other, demonstrating the three-dimensional pathway of smoke transport. It can also be inferred that the smoke layers in the seven cross-sections are capable to represent the different transport phases.~~ Regarding the smoke layers, it can be observed that, during the initial transport ~~phases~~ stages over the continental US on 14 and 15 September, the smoke plumes were accompanied by clouds on their northern sides. The main part of the smoke plume was transported northeast along the HYSPLIT trajectories after 18 September. However, in the cross-sections on 19 and 20 September, a few smoke layers were also identified and observed in the south region with latitudes between 30°N and 40°N, corresponding to the “plume separation” phenomenon found in the analyses of Fig.2 and Fig. ~~5~~6. Only few smoke profiles were determined in this southern pathway, which might result from the smoke plume ~~was~~ being weak, also suggested by the southern branch presented in Fig. 6 (e) and (f) ~~and mixed with dust aerosol~~. In Fig. ~~6~~ 7 (c), the two green curves turning to south could also illustrate the same phenomenon. On 20 and 21 September, the smoke plumes were observed ~~appeared to rise~~ above the cloud layers according to ~~Aeolus~~ ALADIN ~~observations~~data. However, the limited forward trajectory simulations may ~~underestimated~~not adequately represent the ~~height~~ ascending motion of the smoke layer compared to what was observed by ~~the Aeolus~~ ALADIN~~observations~~.

5.1.2 Characteristics of the smoke layers at different transport stages

To characterize better ~~characterize~~ the smoke layers of the different transport ~~phases~~stages, Fig. ~~7~~ 8 presents boxplots of the extinction coefficient, total backscatter coefficient, lidar ratio, aerosol optical depth (AOD), height, and relative humidity of the smoke layers in the cross-sections shown in Fig. ~~6~~7 (a). ~~-~~Only the northern smoke layers (if multiple smoke regions exist, e.g., in the cross-sections of 14, 19 and 20 September) ~~regarded~~ seen in the main smoke plume pathway were selected for the calculation. More statistical results including the mean values and the corresponding standard ~~deviations (std)~~errors the mean (SEM) of these parameters are summarized in Table ~~1~~2. It should be ~~emphasized~~ noted that~~,~~ only Aeolus smoke data bins with an extinction greater than 30 Mm^{-1} and a backscatter greater than 1 $Mm^{-1}sr^{-1}$ were considered representative of smoke layers and used in the statistical calculation. These thresholds are set to filter out low noisy values, which can be observed in the clear sky region of the cross-section presented in Fig.3 (a), so that the remaining values above the threshold are considered representative for the smoke layers. The additional uncertainties of the corrected total backscatter coefficient introduced by the assumed depolarization ratio are discussed in Section 4.3, but are not included in Fig.7 and Table 2.

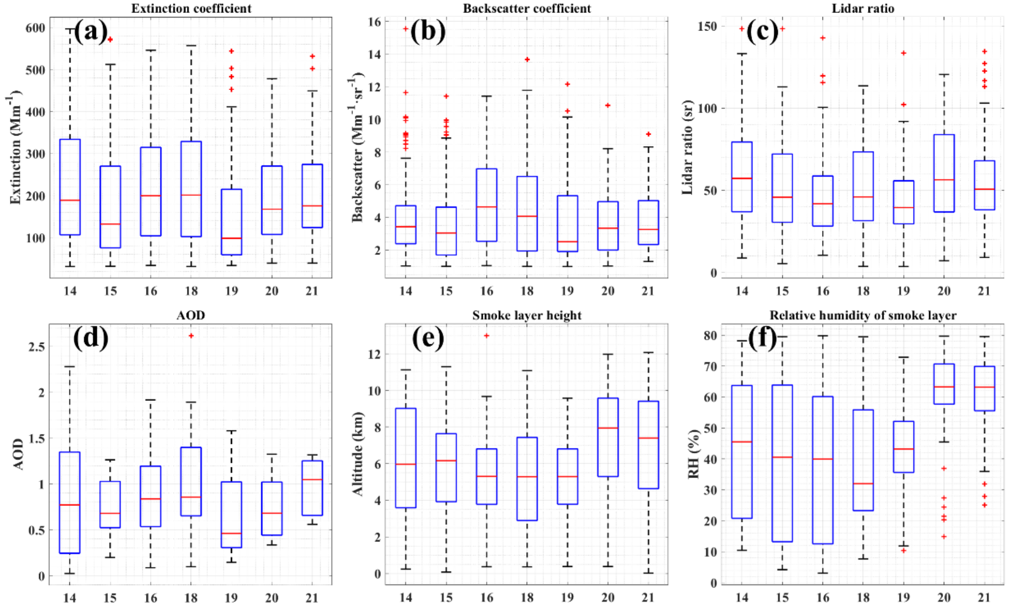

Figure ~~7~~8. The boxplots of (a) extinction coefficient, (b) backscatter coefficient, (c) lidar ratio, (d) AOD, (e) ~~height~~ data bins' altitude and (f) relative humidity of the smoke layers in the cross-sections of Fig. ~~6~~ 7 (a). Only the north smoke layers (if multiple smoke layers exist, e.g., in the cross-section of 14, 19 and 20) ~~regarded~~ seen in the main smoke plume pathway were selected for the calculation.

Table ~~1~~2. Mean values and standard ~~deviations~~ error of the mean (SEM) of extinction coefficient, backscatter coefficient, lidar ratio, AOD, height and relative humidity, of the smoke layers in the cross-sections shown in Fig 6 (a).

Parameter	14/09	15/09	16/09	18/09	19/09	20/09	21/09
Extinction coefficient (Mm^{-1})	231±13~~151~~	175±11~~126~~	221±11~~134~~	220±12~~137~~	155±15~~127~~	199±18~~122~~	208±15~~114~~
Backscatter coefficient (Mm^{-1} • sr^{-1})	4.03±~~2.50~~0.22	3.62±0.20~~2.33~~	5.01±0.22~~2.63~~	4.63±0.25~~2.97~~	3.86±0.35~~2.87~~	3.59±0.29~~1.97~~	3.87±0.24~~1.86~~
Lidar ratio (sr)	62±3.1~~32~~	53±2.5~~28~~	46±2.2~~24~~	52±2.3~~25~~	44±2.9~~24~~	61±4.7~~31~~	58±4.1~~29~~
~~AOD~~	~~0.84±0.65~~	~~0.74±0.32~~	~~0.86±0.41~~	~~1.00±0.61~~	~~0.64±0.44~~	~~0.72±0.33~~	~~0.95±0.31~~
~~Height~~ Altitude (km)	6.14±0.28~~3.13~~	5.63±0.23~~2.7~~	5.29±0.21~~2.39~~	5.23±0.24~~2.78~~	5.25±0.27~~2.22~~	7.19±0.45~~3.12~~	6.89±0.43~~3.31~~
Relative humidity (%)	43±2.0~~22~~	40±2.3~~26~~	38±2.0~~24~~	39±1.8~~21~~	43±1.9~~15~~	60±2.3~~16~~	61±1.7~~13~~

As the extensive properties of aerosols retrieved from the lidar measurements, the extinction coefficient and the backscatter coefficient can represent smoke concentrations. Comprehensively considering the variations in the means and the medians of these two properties during the transport, it can be found that the extensive properties of the smoke layers on 16 and 18 September were obviously higher than those of~~ the preceding and the subsequent~~ cross-sections on 15 and 19 September, indicating higher smoke concentrations. This can also be observed in the cross-sections of 16 and 18 September in Fig. ~~6~~ 7 (a), which include more bins with high extinction values ranging from 300 Mm^{-1} to 400 Mm^{-1} (indicated by yellow). The high smoke concentrations could result from the potential accumulation of smoke aerosols when they were transported to above the Atlantic. This phenomenon agrees well with the findings from the analysis of the MODIS AOD and MERRA-2 smoke CMC across the entire transport region, as illustrated in Fig. 2 (a) and (b) and the accompanying descriptions. On 20 and 21 September, the mean extinction coefficients are 199 Mm^{-1} and 208 Mm^{-1}, and the mean backscatter coefficients are 3.59 Mm^{-1}·sr^{-1} and 3.87 Mm^{-1}·sr^{-1}, which are considered quite high over Europe. In a study targeting a very similar smoke transport event, Hu et al. (2022) reported that a smoke layer transported from the western US was observed by a ground-based lidar over Lille, France, between 22:00 UTC on September 11 and 03:00 UTC on September 12, 2020, with extinction and backscatter coefficients at 355 nm of approximately 180 Mm^{-1} and 5 Mm^{-1}·sr^{-1}, respectively. Similarly, Baars et al. (2021) used a ground-based lidar to detect a smoke layer transported from the western US over Leipzig, Germany, on September 11, 2020, reporting extinction and backscatter coefficients at 355 nm of around 160 Mm^{-1} and 3.3 Mm^{-1}·sr^{-1}. In both cases, the smoke layers were found in the troposphere (5-7 km), which is comparable to the layer heights observed on September 20 and 21 in this study (7.19 km and 6.89 km, respectively). Although these two cases do not describe transport events identical to the one in the present study, they exhibit extinction and backscatter coefficients similar to those observed here, thereby providing some validation for the ALADIN measurements over Europe. Taken together, these findings suggest that dense smoke plumes originating from the western United States covered Europe on September 11, 12, 20, and 21, 2020.

~~-~~As for the variations in the lidar ratio, one of the intensive properties that is independent of aerosol concentrations, it presents the properties of smoke ~~aerosols~~ particles ~~in~~ at different transport ~~phases~~stages. The mean lidar ratios ranged from 44 sr to 62 sr, consistent with the broad range of tropospheric smoke lidar ratios (30-110 sr), summarized in Ansmann et al. (2021). ~~The average lidar ratios present a~~A general declin~~e~~inge ~~tendency~~ trend from 62 sr on 14 September to 44 sr on 19 September was observed ~~,~~ as the smoke transported from the west US to the mid-Atlantic~~ occurred~~. This decline is considered attributed to the aging process of smoke aerosols, aligning with the findings and the statements in Nicolae et al. (2013), Haarig et al. (2018), Nicolae et al. (2026) and Haarig et al. (2026). Taking 44±2.9 sr on 19 September 2020 as the lidar ratio for aged smoke, this value agrees well with the 40-50 sr reported in Baars et al. (2021) and the 40 ± 6 sr reported in Hu et al. (2022) for aged smoke layers from the similar transport event mentioned above. Subsequently, after being transported to Europe and ~~thereby elevated~~appearing ~~over~~ above cloud layers, the mean lidar ratios turned to increase to around 60 sr on 20 and 21 September, ~~which~~ a change that ~~might~~ may be explained by hygroscopic growth~~the changing relative humidity during and after the process of rising~~. During the initial stages of the transport event (14-18 September), the smoke layers gradually became drier, with mean relative humidity from 43 % to 39 %. However, on 20 and 21 September, after the smoke had been transported over Europe and appeared above clouds, the relative humidity of the smoke layers increased to approximately 60%. The lidar ratio and relative humidity exhibited consistent increasing trends on 20 and 21 September. Regarding the extinction coefficient, it increased from 155 Mm^{-1} to around 200 Mm^{-1}, while the backscatter coefficient remained relatively stable. This suggests that the increase in relative humidity enhanced the smoke lidar ratio, given that the lidar ratio is calculated as the extinction coefficient divided by the backscatter coefficient. A similar phenomenon has been observed and discussed for continental aerosols in Haarig et al. (2025).

The smoke layer heights infer the evidence that the layers were primarily in the troposphere during the transport. Regarding the mean values, the decline from 6.14 km on 14 to 5.25 km on 19 September may illustrate that the layers settled slightly during the transport of the high-concentration smoke aerosol. However, 7.19 km on 20 September and 6.89 on 21 September ~~suggest~~ illustrate that these layers were ~~lifted~~ at higher altitudes after being transported to above the Europe. ~~We also provide the relative humidity statistics of the smoke layers to provide ambient information. The smoke layers appear to gradually become drier, with an average relative humidity of 43 % on 14 varying to 39 % on 18. After being separated as the northern portion and lifted above the clouds, the relative humidity of the smoke layers turned out to increase to around 60% on 20 and 21 September, which could be the reason for the altered lidar ratio.~~

In this section, seven descending ~~Aeolus~~ ALADIN measurements were selected to characterize the cross-sections of the smoke plume during the transport. These measurements are considered representative for different transport ~~phases~~ stages of the same plume, as ~~confirmed~~ supported by HYSPLIT trajectory simulations. However, they only provide a limited depiction of the entire smoke plume, which can extend over several thousand kilometers.

5.2 Characteristics of the smoke aerosol plume across its entire transport ~~Features of the entire smoke event~~

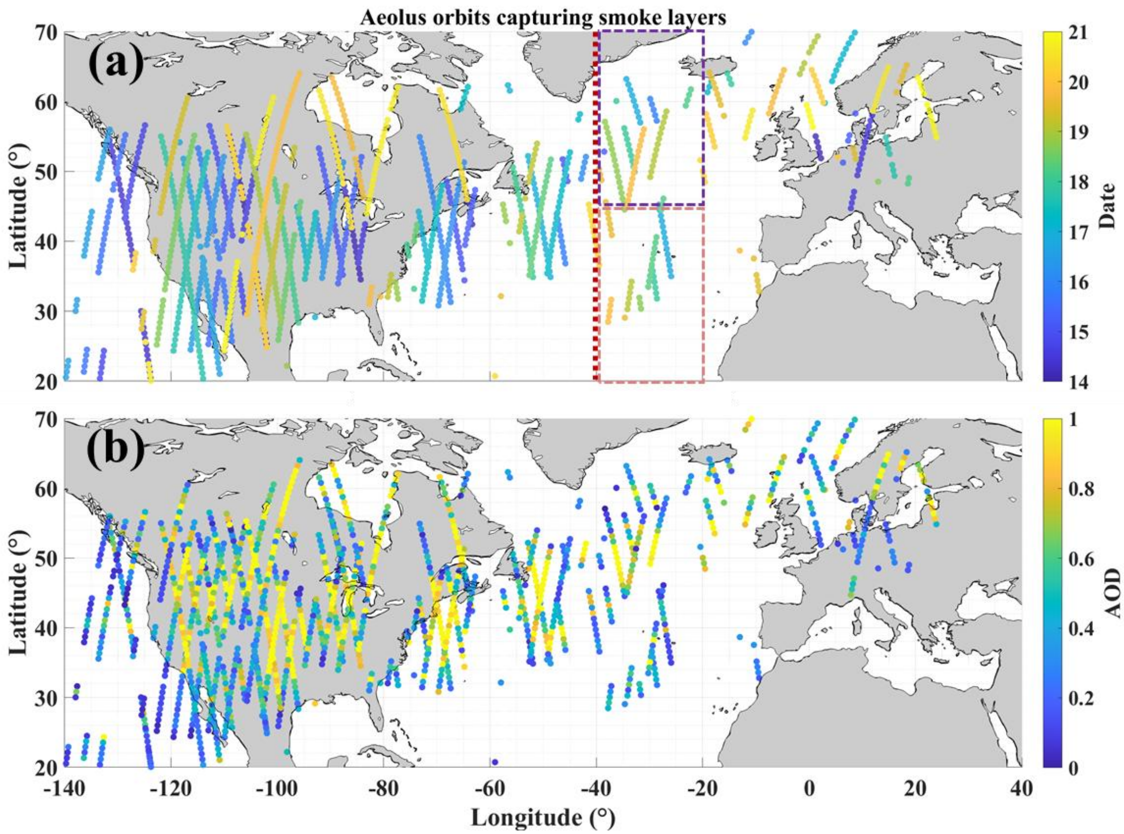

Figure ~~8~~9. Smoke layers captured by ALADIN along the Aeolus orbits, with the color of the tracks representing (a) observational time and (b) AOD. In panel (a), the red dotted line divides the layers at earlier and later transport stage, while the purple and pink dotted boxes highlight the layers of the northern and southern branches following the plume separation.

In this section, all smoke layers identified in the ALADIN measurement cross-sections from 14 to 21 September 2020, within the region from 140°W to 40°E and 20°N to 70°N, are presented together with their statistical results. These analyses aim to investigate the evolution of the entire smoke event throughout its transport pathway. It should be noted firstly, according to the orbit configuration, all data used in this section were located close to the terminator but in illuminated regions (ESA, 2008).

Accordingly, no differences are expected between data from ascending and descending orbits.

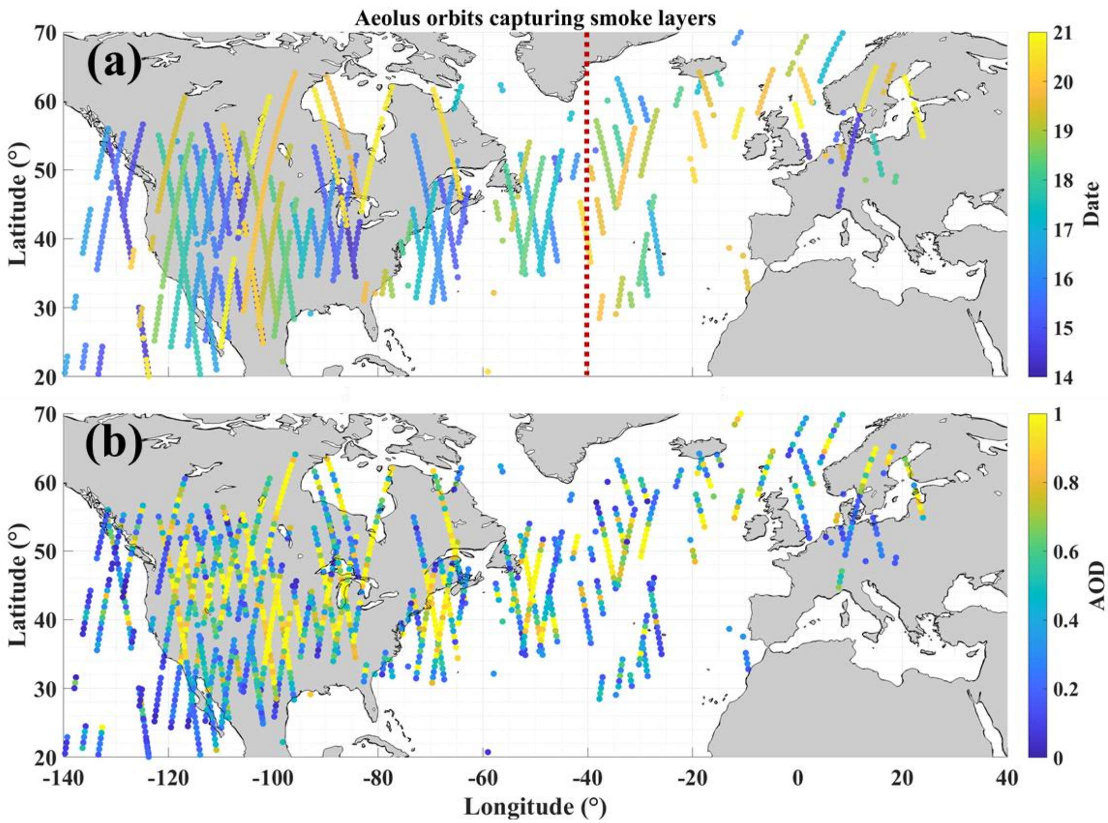

Figure ~~8~~ 9 shows the smoke layers captured by ALADIN. The colors in the panel (a) indicate the observational time from 14 to 21 September 2020, while the colors in the panel (b) show the smoke AOD. Firstly, ~~it can be found that the~~ panel (a) is ~~separated~~ divided by a red dotted line. In the left side of the dotted line, it can be seen that blue and green tracks dominate the region of 140°W to 40°W. This illustrates that the smoke plumes were observed in this region from 14 to 18 September, suggesting that the smoke plumes were transported there during this period. There are also several yellow tracks in the continental US region, indicating that smoke aerosols were still being generated by wildfires from 19 to 21 September. ~~However, they were spread above the land but they might not have been transported to the Atlantic.~~ To the right of the red dotted line, more yellow orbits appear from the mid-Atlantic region to northern Europe, implying the smoke plume moved along this pathway from 19 to 21 September. Several deep blue dots also appear there, suggesting that before 14 September, the smoke layers may have been transported from North America. It can be also clearly found that the smoke plume separated above the mid-Atlantic around 18 to 19 September. The movement of the smoke plume observed by Aeolus aligns well with the smoke CMC maps shown in Fig. ~~5~~6. Although daily MODIS AOD can provide photo-like observations of smoke plumes over large horizontal regions, they are quite cloud-sensitive that the smoke plume above the northern Europe on 20 and 21 September cannot be recorded due to the cloud cover (shown in Fig. A1). We believe that Aeolus ~~lidar observations~~ smoke dataset acquired in this paper ~~are~~ is capable ~~to~~ of ~~identify~~ observing a smoke layer even if ~~thin~~ clouds are present below the smoke layers in a given profile. As shown in panel (b) of Fig. ~~8~~9, several high AOD values were observed above Northern Europe. In general, the bright yellow colors in the panel (b) indicate the main pathway of the smoke plume. The separated southern smoke plume, with the major AOD below 0.6, is inferred to be weaker than the northern one. The reason that Aeolus smoke dataset does not present the transport of the southern plume near the Sahara Desert could be ~~because~~ that the plume ~~it~~ is mixed with dust aerosols, ~~which results in~~leading to its exclusion from the dataset, as described in Section 4.2.

To ~~further quantitatively~~ characterize the features of the smoke event during transport more quantitively, the statistic~~s of the AOD, layer altitude,~~al results (AOD, altitudes and lidar ratio) ~~extinction coefficient and lidar ratio were~~will be ~~calculated~~ analysed along the longitude ~~and altitude~~ in the following~~, shown in Fig. 9 through Fig. 11, respectively~~. Regarding AOD and lidar ratio, Aeolus smoke data bins within the altitude range of 2 km to 12 km were selected for the ~~analysis~~statistics. The chosen altitude range was selected because (1) this smoke transport event occurred mainly below 12 km (see Fig. ~~7e~~8 (e)), which approximately corresponds to the typical tropopause height in mid-latitudes, and (2) it minimizes the influence of other aerosol types present in the planetary boundary layer (e.g., continental pollution and marine aerosols).~~-~~ In ~~addition~~addition~~, for all parameters except AOD~~, only the data bins with extinction greater than 30 Mm^{-1} and backscatter greater than 1 $Mm^{-1}sr^{-1}$ were considered representative of smoke layers and used in the statistical calculation. These thresholds are set to filter out low noisy values, which can be observed in the clear sky region of the cross-section presented in Fig.3 (a), so that the remaining values above the threshold are considered representative for the smoke layers. Since the entire smoke plume moved eastward, the statistical values along the longitude are likely to reflect the characteristics of the smoke event along its transport pathway.

5.2.1 Variation of smoke aerosol optical depth and altitude along the longitude

In Fig. 10~~9~~, using the Aeolus smoke dataset in the period of 14 to 21 September 2020, in the smoke plume transport region of 140°W to 40°E and 20°N to 70N, the means and the standard deviations of AOD (panel (a)) and altitude (panel (b)) were calculated with the longitude grid of 20°. The corresponding data counts are shown in panels (c) and (d).

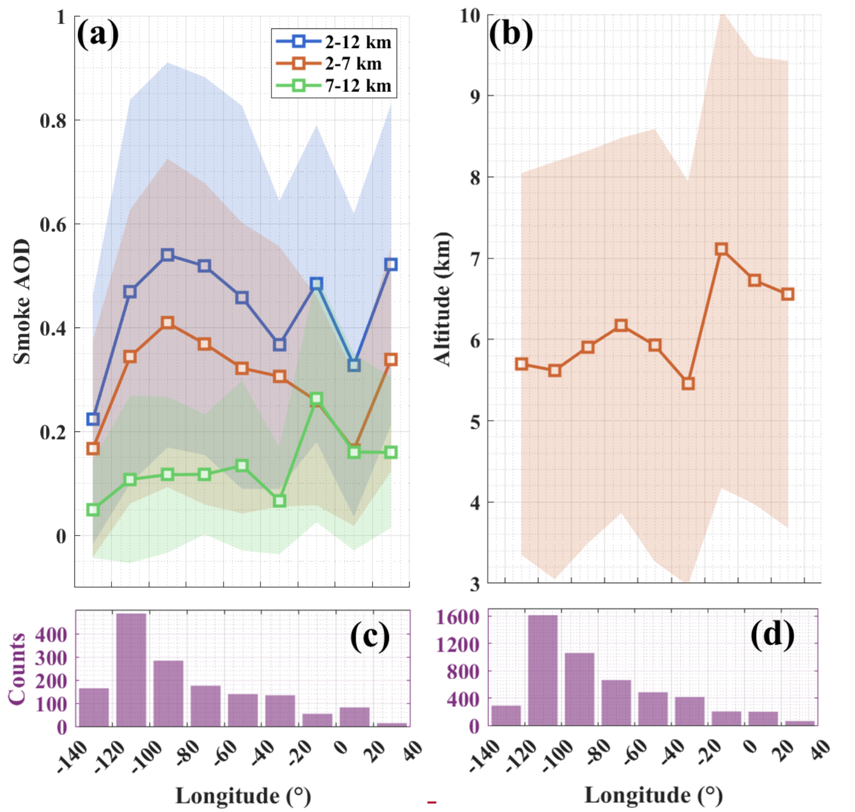
(a)
2-12 km
2-7 km
7-12 km
Smoke AOD
1
0.8
0.6
0.4
0.2
0
(b)
Altitude (km)
10
9
8
7
6
5
4
3
(c)
Counts
400
300
200
100
0
(d)
1600
1200
800
400
0
-140
-120
-100
-80
-60
-40
-20
0
20
40
Longitude (°)
Longitude (°)

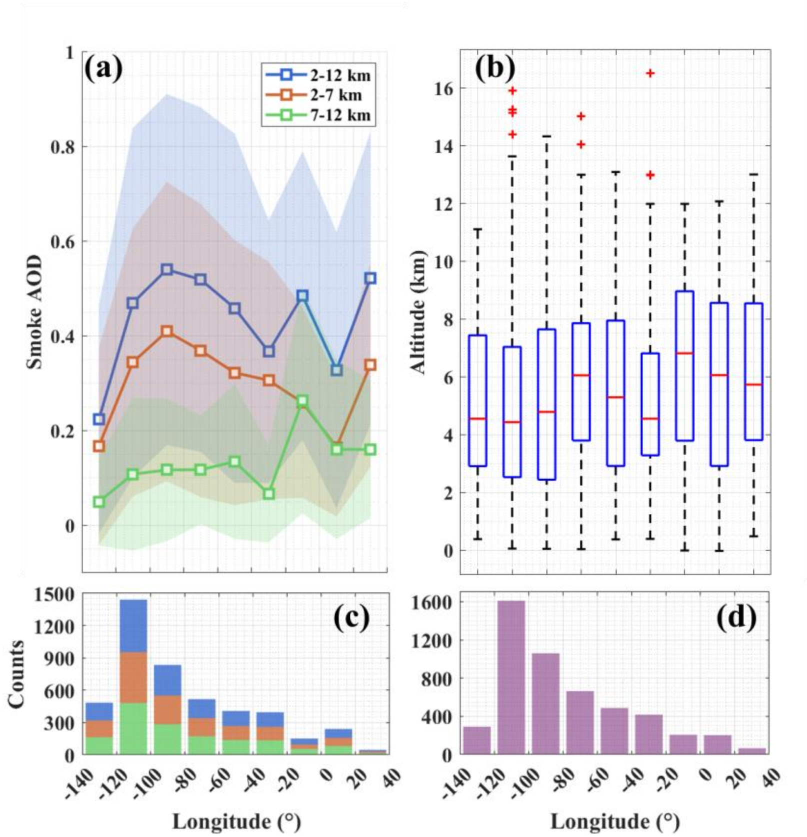

Figure ~~9~~10. Statistical results ~~(means and standard deviations) of~~ (a) smoke AOD (means and standard deviations), (b) smoke bins ~~lidar ratio and~~ altitude (boxplot) along longitude. (c)(d) The corresponding data counts of the statistics. The statistics were calculated ~~by~~ using the Aeolus smoke dataset ~~(within the altitude range of 2 km to 12 km)~~ in the period of 14 to 21 September 2020, in the smoke plume transport region of 140°W to 40°E and 20°N to 70N, and with the longitude grid of 20°. Smoke AOD includes total AOD (2 km to 12 km), AOD within 2 to 7 km (AOD_M), and AOD within 7 to 12 km (AOD_U), indicated by the blue, red and green curves, respectively. In panel (c), the corresponding data counts are also presented by the stacked bars in the same color with the AOD curves.

In panel (a), we present the variations of total AOD (2 km to 12 km), AOD within 2 to 7 km (AOD_M, corresponding to the mid-troposphere) and AOD within 7 to 12 km (AOD_U, corresponding to the upper-troposphere), indicated by the blue, red and green curves individually. In general, the total AOD exhibits a declininge tendency, dropping from around 0.54 to below 0.33 in the main transport region between 100°W and 20°E. Combining the declining trend in AOD from the Copernicus Atmosphere Monitoring Service model-from 0.5 over the western United States to 0.2 over Europe-during a similar smoke transport event in September 2020 reported by Ceamanos et al. (2023), and comparing both this event and the current study with a tropospheric transatlantic smoke transport event in 2019 from Canada to Europe, where AOD declined from 0.25 to 0.013 as reported by Shang et al. (2024), it can be inferred that the September 2020 smoke transport event was fairly severe. The AOD_M shows a similar trend, suggesting that the smoke layers in the mid-troposphere weaken during transport. Additionally, the sharp increases in AOD and AOD_M may be attributed to the low data count (15), which are considered insufficient to be representative of the observed trend. However, for the AOD_U, the slight increasing trend within 120°W to 40°W indicates that a few smoke aerosols were ~~injected~~ lofted into the upper-troposphere from the mid-troposphere while the smoke plume was being transported into this region. The relatively large decline in AOD_U, from around 0.13 to below 0.07, occurred after plume separation in the region of 40°W to 20°W. After being transported above Europe, the AOD_U increased rapidly to around 0.26 in the region of 20°W to 0°. Regarding to medians of the ~~average~~ altitudes, basically, they show an ascending trend from around ~~5.6~~4.4 km to ~~around~~ exceeding ~~6~~ 5.3 km in the region of 140°W to 40°W, which corresponds to the increasing AOD_U in this region. A descent to ~~below~~ around ~~5~~4.5 km appeared in the plume separation region between 40°W and 20°W. Subsequently, the ~~average~~ altitude medians~~s~~ turned to increase to over ~~7.1~~6 km upon reaching Europe. Comprehensively considering the variations in both average AOD and altitude along the transport pathway, it can be inferred that the smoke plume was generally located below 12 km (the typical tropopause height at mid-latitudes), with its intensity weakening and its altitude rising~~considering the variations in the average AOD and altitude along the smoke transport pathway, it can be inferred that, in general, the smoke plume within 2 km to 12 km (typical altitude range of free troposphere) was weaken but lifted~~.

Nevertheless, distinct weakened ~~abnormal~~ tendencies of AOD_U and layer altitude occurred in the region of 40°W to 20°W, which may be related to the ~~mechanism~~process of the plume separation, indicated by two branches of the smoke layers captured by ALADIN within the purple and pink dotted boxes in Fig.8(a), individually. For further investigation, the statistical analyses are conducted targeting these two boxes in the following.

5.2.2 Investigation of the two branches following plume separation

Integrating the ALADIN smoke observations within the purple and pink dotted boxes in Fig.8(a), representing the two branches following the plume separation, the smoke AOD and layer altitudes of both branches are investigated by statistical analyses.

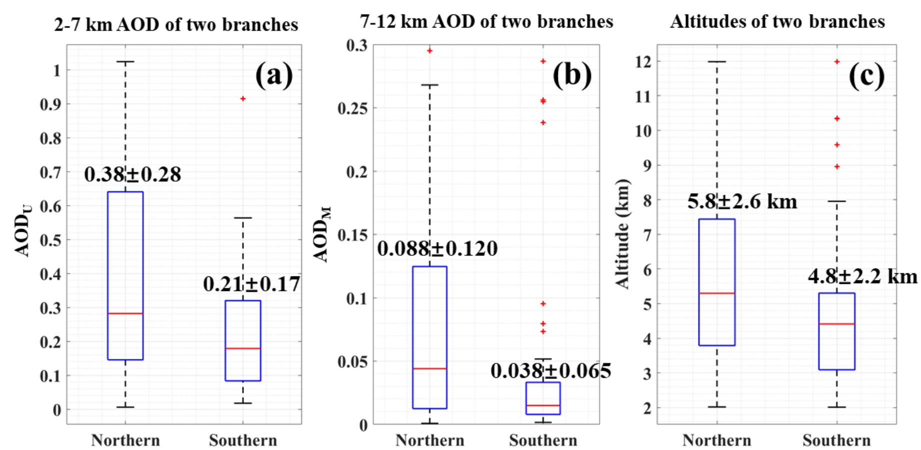

Figure 11 Statistical results of the two branches following the plume separation calculated from ALADIN smoke observations within the purple dotted box (latitude 45°N-70°N, longitude 40°W-20°W) and the pink dotted box (latitude 20°N-45°N, longitude 40°W-20°W) in Fig.8(a), labelled "Northern" and "Southern". (a) 2-7 km AOD (AOD_U) of two branches; (b) 7-12 km AOD (AOD_M) of two branches; (c) Layer altitudes of two branches.

Figure 11 presents the statistical results (boxplots, mean values, and corresponding standard deviations) of the two branches following the plume separation calculated from ALADIN smoke observations within the purple dotted box (latitude 45°N-70°N, longitude 40°W-20°W) and the pink dotted box (latitude 20°N-45°N, longitude 40°W-20°W) in Fig.8(a), labelled "Northern" and "Southern," respectively. AOD_U, AOD_M, and layer altitudes are presented in panel (a), (b) and (c), respectively. Overall, the smoke aerosol load in the northern branch was higher than that in the southern branch. The notably low AOD_M of the southern branch, with a mean value of 0.038 and a median of 0.015, contributed to the distinctly low AOD_M observed in the region between 40°W to 20°W, as shown in Fig.9(a). Regarding layer altitudes, the northern branch was situated higher than the southern one. The southern branch, with a mean altitude of 4.8 km and a median of 4.4 km, is considered be responsible for the low altitude in the same (40°W to 20°W) depicted in Fig.9 (a). The information from Fig.11 provides insights into the behaviour of the two branches following the plume separation: the stronger and higher northern branch was subsequently transported toward Europe, while the southern branch was weaker and became lower in altitude.

5.2.3 Variation of lidar ratio along the longitude

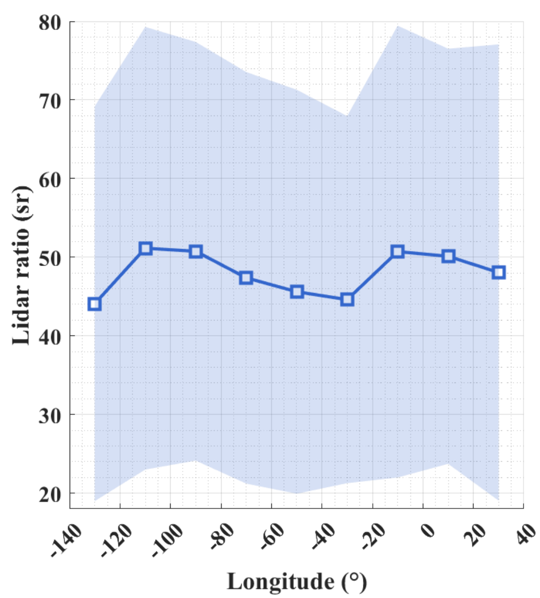

Figure ~~10~~12. Statistical results (means and standard deviations) of smoke lidar ratio along longitude. The statistics were calculated by using the Aeolus smoke dataset (within the altitude range of 2 km to 12 km) in the period of 14 to 21 September 2020, in the smoke plume transport region of 140°W to 40°E and 20°N to 70N, and with the longitude grid of 20°.

Figure ~~10~~ 12 shows the variation in the smoke lidar ratio along longitude. ~~Basically~~Overall, the mean lidar ratio, ranginge ~~of~~ from 44 sr to 51 sr, fall within the ~~is reasonable~~ typical range for smoke aerosols (~~Floutsi~~ Ansmann et al., ~~2023~~2021), though it exhibits less variability compared to the selected cross-sections (44 sr to 62 sr) discussed in Section 5.2.1. Initially, the mean values decrease from over 50 sr ~~in~~ over the continental US (120°W to 80°W) to around 45 sr over the mid-Atlantic (60°W to 20°W). Subsequently, they turned to rise to nearly 50 sr ~~after~~ upon reaching Europe. The decreasing-increasing trend is consistent with the findings in Section 5.2.1, and could also be explained by the aging process of smoke particles followed by hygroscopic growth (Haarig et al., 2025; Haarig et al., 2026). ~~It should be noted that the lowest mean lidar ratio, 44.6 sr, appeared in the region of 40°W to 20°W, which may also be related to the plume separation.~~ The impact of the backscatter correction, based on an assumed constant depolarization ratio, on the smoke lidar ratio has been discussed in Section 4.~~2~~3. A variation in the mean depolarization ratio of approximately 0.01 at different transport stages could result in a lidar ratio variation of about 0.9 sr, which has a negligible effect on the overall lidar ratio variation. Therefore, the mean lidar ratio shown in Fig. 12 is considered representative of the entire smoke transport event along the pathway.~~A mean depolarization ratio variation of around 0.01 could induce a lidar ratio variation of around 1 sr, which has a negligible impact on the total lidar ratio variation. Thus, it is considered that the mean lidar ratio shown in Fig. 10 is capable to be representative of the property variation of the smoke event along the transport pathway.~~

6 Summary and outlook

Spaceborne lidar observations are well suited for studying the large-scale aerosol transport, because they have the potential to acquire cross-sections of aerosol plume during different transport ~~phases~~stages. Although the Atmospheric Laser Doppler Instrument (ALADIN) onboard the Aeolus satellite was designed as a wind measurement lidar, it ~~has been~~is capable of providing aerosol profiles as a high spectral resolution lidar. These profiles can be used to investigate aerosol transport.

In this study, targeting the wildfire season of the West Coast of the US in September 2020, a comprehensive investigation of transatlantic transport of smoke generated by intense fires~~on an intense transatlantic smoke transport~~ was conducted, based on the ~~Aeolus~~ ALADIN observation, ~~synergic~~ in synergy with another spaceborne lidar CALIOP (Cloud-Aerosol Lidar with Orthogonal Polarization), spaceborne passive instruments (Visible Infrared Imaging Radiometer Suite, VIIRS; Moderate-resolution Imaging Spectroradiometer, MODIS) and models (Modern-Era Retrospective analysis for Research and Applications, Version 2, MERRA-2; Hybrid Single Particle Lagrangian Integrated Trajectory Model, HYSPLIT). The smoke plume transport event was determined starting from the west coast of the US on around 14 September, crossing the Atlantic, finally arriving above the Europe on 21 September. In order to derive a smoke dataset of extinction coefficient, backscatter coefficient and lidar ratio from Aeolus, a collocation dataset comprising Aeolus ~~observations~~products, MODIS AOD, and MERRA-2 smoke column mass concentration (CMC) was established. Subsequently, the method for ~~the derivation of~~ deriving smoke data from ALADIN observations was highlighted, including 1) ~~bins selection~~quality control, 2) cloud screening, 3) smoke profile selection, 4) backscatter coefficient correction and 5) lidar ratio calculation. The reliability of the Aeolus smoke dataset was validated by the comparison of AOD with MODIS measurement.

In terms of the characterization of the smoke transport, seven cross-sections on 14, 15, 16, 18, 19, 20 and 21 September, located from the west of the US eastwards to the Europe, were ~~preliminarily~~ selected as the first case. HYSPLIT trajectory simulations have been used to support the representativeness of these cross-sections for the smoke transport event. The specific transport pathway was described in detail by the vertical structure within these cross-sections~~these cross-sections with vertical structure~~.

The potential smoke aerosol accumulation during the transport was observed in the cross-sections on 16 and 18 September, corresponding well to the AOD and CMC maps. That smoke layers appeared above cloud layers over Europe was implied by the cross-sections on 20 and 21 September. Statistics of each cross-sections were also presented and analysed. Moreover, the features of the entire smoke plume during transport were investigated using the Aeolus smoke dataset from 14 to 21 September 2020, in the transport region. This dataset included all smoke layers captured by Aeolus along its orbits. We highlight the capability of the Aeolus smoke dataset (derived from ALADIN with the assistance of multi-source data) to observe aerosol layers above clouds, thereby providing more information than passive instruments such as MODIS, which are susceptible to cloud contamination.~~We highlight the ability of Aeolus to measurement aerosol layers even if in the presence of thin clouds, providing more information than passive instruments like MODIS, which are sensitive to cloud contamination.~~ Based on the Aeolus smoke dataset, we further characterized the smoke plumes along the transport pathway using statistics of AOD, altitude, and lidar ratio. Additionally, the plume separation that occurred between 40°W and 20°W was investigated. Based on a comprehensive consideration of all results, the key features of the smoke transport event are summarized as follows: ~~In general, the AOD decreased along the pathway as the smoke plume dispersed during transport. In addition, the growing AOD in the upper-troposphere (AOD_U, at altitudes ranging from 7 km to 12 km) and the ascending layer altitudes along the longitude both indicates the smoke plume was gradually lifted during transport. The mean lidar ratios were within a reasonable range of 44 sr to 51 sr for smoke aerosol, showing a general decreasing-increasing trend along the transport pathway. Notably, the lowest values of AOD_U, layer altitude and lidar ratio along the main pathway (120°W to 40°W) appeared within the region of 40°W to 20°W. This may be related to the plume separation that occurred in this region.~~

1. The smoke plume remained fairly intense throughout the transport. The mean extinction coefficients on the seven selected cross-sections at different stages were all approximately 200 Mm^{-1}. The AOD (integrated between 2 km and 12 km altitude) decreased from 0.54 above the US to 0.33 above Europe.

2. The plume was transported primarily below 12 km. The median layer altitudes ascended from approximately 4.4 km to over 6 km. Additionally, the smoke layers appeared above clouds when transported to Europe.

3. As revealed by the cross-sections, the declining trend of the lidar ratio from 62 sr on 14 September to 44 sr on 19 September can be explained by the aging process of smoke aerosols. Subsequently, the increase to approximately 60 sr on 20 and 21 September was found to be related to the hygroscopic growth of smoke particles.

4. Plume separation was observed during transport between 40°W and 20°W. Following the separation, the stronger and higher northern branch was subsequently transported toward Europe, while the southern branch was weaker and remained at a lower altitude.

In conclusion, we demonstrated that Aeolus can provide reliable observation of smoke transport event with the synergy of multi-platform data. We believe that the characteristic aerosol properties during a long-range smoke transport event~~comprehensive characterization of this large-scale transatlantic smoke transport event~~ by a spaceborne high spectral resolution lidar (HSRL) provides valuable information for global aerosol research, particularly highlighting the capabilities of ~~lidars~~ the HSRL to provide ~~vertically resolved information~~lidar ratio retrieval. In the future, the synergy of multi-spaceborne

HSRL missions (the Aerosol and Carbon Detection Lidar (ACDL) at 532 nm, the ATmospheric LIDar (ATLID) at 355 nm, and the wind and aerosol lidar onboard the future Aeolus follow-on mission) has great potential for the large-scale aerosol transport research with muti-wavelength observations and dynamic field measurements (Dai et al., 2024; Donovan et al., 2024).

Appendix

~~Longitude ranges of Sub-regions~~	~~140°W - 120°W~~	~~120°W - 100°W~~	~~100°W -80°W~~	~~80°W-60°W~~	~~60°W-40°W~~	~~40°W-20°W~~	~~20°W-0°~~	~~0°-20°W~~	~~20-40°W~~
~~Depolarization ratio (mean ± std)~~	~~0.119± 0.087~~	~~0.117± 0.088~~	~~0.119± 0.088~~	~~0.114± 0.088~~	~~0.116± 0.087~~	~~0.111± 0.083~~	~~0.110± 0.083~~	~~0.110± 0.085~~	~~0.116± 0.086~~

~~**Table A1. Depolarization ratio at 532 nm of the smoke plume during transport from 140°to 40°E, derived from CALIOP observations.**~~

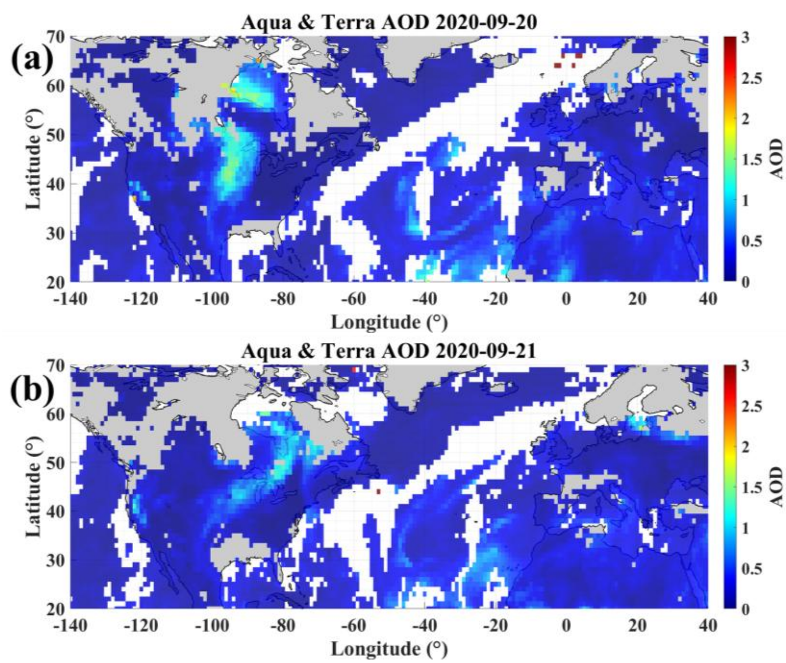

Figure A1. Average AOD from both Aqua and Terra on (a) 20 and (b) 21 September 2020.

Data availability

The Aeolus data were downloaded via the website https://aeolus-ds.eo.esa.int/oads/access (last access: 1 February 2026). The CALIOP data were downloaded from https://www.earthdata.nasa.gov (last access: 1 February 2026). The VIIRS products were acquired from https://worldview.earthdata.nasa.gov (last access: 1 February ~~2025~~2026). Data from MODIS and MERRA-

2 were downloaded via https://giovanni.gsfc.nasa.gov/giovanni (last access: 1 February 2026). The HYSPLIT models were conducted in the website https://www.ready.noaa.gov/hypub-bin/trajtype.pl?runtype=archive (last access: 1 February 2026).

Author contribution

SW, KS and GD conceived the study; KS conducted the experiments and wrote the manuscript; DT and HB contributed to the data analysis; all co-authors discussed the results and revised the manuscript.

Competing interests

The authors declare that they have no conflict of interest.

Funding

This research was jointly funded by the National Key Research and Development Program of China, grant number 2024YFF0726403, the National Natural Science Foundation of China, grant number 42475145 and U2106210, and the Hainan Province Science and Technology Special Fund, grant number ZDYF2024GXJS012.

Acknowledgements

We appreciate the enormous effort of Aeolus team under the frame of Aeolus DISC (Data, Innovation, and Science Cluster), who are still working on the validation and refinement of ALADIN data. This study was also supported by the Dragon 6 program, which is conducted by the European Space Agency and the China Science and Technology Exchange Center (grant no. 95376). Kangwen Sun appreciates the support from the China Scholarship Council (CSC) to conduct this research under the CSC no. 202306330054.

References

Abril-Gago, J., Guerrero-Rascado, J. L., Costa, M. J., Bravo-Aranda, J. A., Sicard, M., Bermejo-Pantaleón, D., Bortoli, D., Granados-Muñoz, M. J., Rodríguez-Gómez, A., Muñoz-Porcar, C., Comerón, A., Ortiz-Amezcua, P., Salgueiro, V., Jiménez-Martín, M. M., and Alados-Arboledas, L.: Statistical validation of Aeolus L2A particle backscatter coefficient retrievals over ACTRIS/EARLINET stations on the Iberian Peninsula, Atmos. Chem. Phys., 22, 1425–1451, https://doi.org/10.5194/acp-22-1425-2022, 2022.

Ansmann, A., Wandinger, U., Le Rille, O., Lajas, D., and Straume, A. G.: Particle backscatter and extinction profiling with the spaceborne high-spectral-resolution Doppler lidar ALADIN: methodology and simulations, Appl. Optics, 46, 6606, https://doi.org/10.1364/AO.46.006606, 2007.

Ansmann, A., Ohneiser, K., Mamouri, R.-E., Knopf, D. A., Veselovskii, I., Baars, H., Engelmann, R., Foth, A., Jimenez, C., Seifert, P., and Barja, B.: Tropospheric and stratospheric wildfire smoke profiling with lidar: mass, surface area, CCN, and INP retrieval, Atmos. Chem. Phys., 21, 9779–9807, https://doi.org/10.5194/acp-21-9779-2021, 2021.

Ansmann, A., Jimenez, C., Roschke, J., Bühl, J., Ohneiser, K., Engelmann, R., Radenz, M., Griesche, H., Hofer, J., Althausen, D., Knopf, D. A., Dahlke, S., Gaudek, T., Seifert, P., and Wandinger, U.: Impact of wildfire smoke on Arctic cirrus formation – Part 1: Analysis of MOSAiC 2019–2020 observations, Atmos. Chem. Phys., 25, 4847–4866, https://doi.org/10.5194/acp-25-4847-2025, 2025.

Ångström, A. (1964), The parameters of atmospheric turbidity. Tellus, 16: 64-75. https://doi.org/10.1111/j.2153-3490.1964.tb00144.x

Baars, H., Ansmann, A., Ohneiser, K., Haarig, M., Engelmann, R., Althausen, D., Hanssen, I., Gausa, M., Pietruczuk, A., Szkop, A., Stachlewska, I. S., Wang, D., Reichardt, J., Skupin, A., Mattis, I., Trickl, T., Vogelmann, H., Navas-Guzmán, F., Haefele, A., Acheson, K., Ruth, A. A., Tatarov, B., Müller, D., Hu, Q., Podvin, T., Goloub, P., Veselovskii, I., Pietras, C., Haeffelin, M., Fréville, P., Sicard, M., Comerón, A., Fernández García, A. J., Molero Menéndez, F., Córdoba-Jabonero, C., Guerrero-Rascado, J. L., Alados-Arboledas, L., Bortoli, D., Costa, M. J., Dionisi, D., Liberti, G. L., Wang, X., Sannino, A., Papagiannopoulos, N., Boselli, A., Mona, L., D'Amico, G., Romano, S., Perrone, M. R., Belegante, L., Nicolae, D., Grigorov, I., Gialitaki, A., Amiridis, V., Soupiona, O., Papayannis, A., Mamouri, R.-E., Nisantzi, A., Heese, B., Hofer, J., Schechner, Y. Y., Wandinger, U., and Pappalardo, G.: The unprecedented 2017–2018 stratospheric smoke event: decay phase and aerosol properties observed with the EARLINET, Atmos. Chem. Phys., 19, 15183–15198, https://doi.org/10.5194/acp-19-15183-2019, 2019.

Baars, H., Radenz, M., Floutsi, A. A., Engelmann, R., Althausen, D., Heese, B., et al. (2021). Californian wildfire smoke over Europe: A first example of the aerosol observing capabilities of Aeolus compared to ground-based lidar. Geophysical Research Letters, 48, e2020GL092194. https://doi. org/10.1029/2020GL092194.

Beer, C. G., Hendricks, J., and Righi, M.: A global climatology of ice-nucleating particles under cirrus conditions derived from model simulations with MADE3 in EMAC, Atmos. Chem. Phys., 22, 15887–15907, https://doi.org/10.5194/acp-22-15887-2022, 2022.

Beer, C. G., Hendricks, J., and Righi, M.: Impacts of ice-nucleating particles on cirrus clouds and radiation derived from global model simulations with MADE3 in EMAC, Atmos. Chem. Phys., 24, 3217–3240, https://doi.org/10.5194/acp-24-3217-2024, 2024.

Buchard, V., and Coauthors, 2017: The MERRA-2 Aerosol Reanalysis, 1980 Onward. Part II: Evaluation and Case Studies. J. Climate, 30, 6851–6872, https://doi.org/10.1175/JCLI-D-16-0613.1.

Ceamanos, X., Coopman, Q., George, M. et al. Remote sensing and model analysis of biomass burning smoke transported across the Atlantic during the 2020 Western US wildfire season. Sci Rep 13, 16014 (2023). https://doi.org/10.1038/s41598-023-39312-1.

Chipade, R.A.; Pandya, M.R. Theoretical derivation of aerosol lidar ratio using Mie theory for CALIOP-CALIPSO and OPAC aerosol models. Atmos. Meas. Tech. 2023, 16, 5443–5459.

Cunningham, C., Williamson, G., and Bowman, D.: Increasing frequency and intensity of the most extreme wildfires on Earth, Nat. Ecol. Evol., 12, 1420–1425, https://doi.org/10.1038/s41559-024-02452-2, 2024.

Dabas, A., Denneulin, M. L., Flamant, P., Loth, C., Garnier, A., and Dolfi-Bouteyre, A.: Correcting winds measured with a Rayleigh Doppler lidar from pressure and temperature effects, Tellus A, 60, 206–215, https://doi.org/10.1111/j.1600-0870.2007.00284.x, 2008.

Dai, G., Wu, S., Long, W., Liu, J., Xie, Y., Sun, K., Meng, F., Song, X., Huang, Z., and Chen, W.: Aerosol and cloud data processing and optical property retrieval algorithms for the spaceborne ACDL/DQ-1, Atmos. Meas. Tech., 17, 1879–1890, https://doi.org/10.5194/amt-17-1879-2024, 2024.

Ditas, J., Ma, N., Zhang, Y., Assmann, D., Neumaier, M., Riede, H., Karu, E., Williams, J., Scharffe, D., Wang, Q., Saturno, J., Schwarz, J. P., Katich, J. M., McMeeking, G. R., Zahn, A., Hermann, M., Brenninkmeijer, C. A. M., Andreae, M. O., Pöschl, U., Su, H., and Cheng, Y.: Strong impact of wildfires on the abundance and aging of black carbon in the lowermost stratosphere, P. Natl. Acad. Sci. USA, 115, E11595-E11603, https://doi.org/10.1073/pnas.1806868115, 2018.

Donovan, D. P., van Zadelhoff, G.-J., and Wang, P.: The EarthCARE lidar cloud and aerosol profile processor (A-PRO): the A-AER, A-EBD, A-TC, and A-ICE products, Atmos. Meas. Tech., 17, 5301–5340, https://doi.org/10.5194/amt-17-5301-2024, 2024.

Eck, T. F., Holben, B. N., Reid, J. S., Sinyuk, A., Giles, D. M., Arola, A., Slutsker, I., Schafer, J. S., Sorokin, M. G., Smirnov, A., LaRosa, A. D., Kraft, J., Reid, E. A., O'Neill, N. T., Welton, E. J., and Menendez, A. R.: The extreme forest fires in California/Oregon in 2020: Aerosol optical and physical properties and comparisons of aged versus fresh smoke, Atmos. Environ., 305, 119798, https://doi.org/10.1016/j.atmosenv.2023.119798, 2023.

Eggers, N., Graßl, S., & Ritter, C. (2024). Assessment of Hygroscopic Behavior of Arctic Aerosol by Contemporary Lidar and Radiosonde Observations. Remote Sensing, 16(16), 3087. https://doi.org/10.3390/rs16163087

Ehlers, F., Flament, T., Dabas, A., Trapon, D., Lacour, A., Baars, H., and Straume-Lindner, A. G.: Optimization of Aeolus' aerosol optical properties by maximum-likelihood estimation, Atmos. Meas. Tech., 15, 185–203, https://doi.org/10.5194/amt-15-185-2022, 2022.

Eitan Hirsch, Ilan Koren, Record-breaking aerosol levels explained by smoke injection into the stratosphere. Science371,1269-1274(2021).DOI:10.1126/science.abe1415.

ESA: ADM-Aeolus Science Report, ESA SP-1311, 121 pp., European Space Agency, ISBN 978-92-9221-404-3, https://esamultimedia.esa.int/multimedia/publications/SP-1311/SP-1311.pdf (last access: 22 May 2026), 2008.

Flamant, P. H., Cuesta, J., Denneulin, M.-L., Dabas, A., and Huber, D.: ADM-Aeolus retrieval algorithms for aerosol and cloud products, Tellus A, 60, 273–286, https://doi.org/10.1111/j.1600-0870.2007.00287.x, 2008.

Flamant, P., Dabas, A., Martinet, P., Lever, V., Flament, T., Trapon, D., Olivier, M., Cuesta, J., and Huber, D.: Aeolus L2A Algorithm Theoretical Baseline Document, Particle optical properties product, Tech. rep., ESA, version 6.0, https://earth.esa.int/eogateway/documents/20142/37627/Aeolus-L2A-Algorithm-Theoretical-Baseline-Document.pdf (last access: 28 May 2026), 2022.

Flament, T., Trapon, D., Lacour, A., Dabas, A., Ehlers, F., and Huber, D.: Aeolus L2A aerosol optical properties product: standard correct algorithm and Mie correct algorithm, Atmos. Meas. Tech., 14, 7851–7871, https://doi.org/10.5194/amt-14-7851-2021, 2021.

Floutsi, A. A., Baars, H., Engelmann, R., Althausen, D., Ansmann, A., Bohlmann, S., Heese, B., Hofer, J., Kanitz, T., Haarig, M., Ohneiser, K., Radenz, M., Seifert, P., Skupin, A., Yin, Z., Abdullaev, S. F., Komppula, M., Filioglou, M., Giannakaki, E., Stachlewska, I. S., Janicka, L., Bortoli, D., Marinou, E., Amiridis, V., Gialitaki, A., Mamouri, R.-E., Barja, B., and Wandinger, U.: DeLiAn – a growing collection of depolarization ratio, lidar ratio and Ångström exponent for different aerosol types and mixtures from ground-based lidar observations, Atmos. Meas. Tech., 16, 2353–2379, https://doi.org/10.5194/amt-16-2353-2023, 2023.

Foken, T. Springer Handbook of Atmospheric Measurements, 1st ed.; Springer: Cham, Switzerland, 2021. https://doi.org/10.1007/97 8-3-030-52171-4.

Forbes, R. M. Ahlgrimm, O. Stiller, S. Di Michele and J. Delanoe, 2009: Validation of cloud parametrization. WP-2100 report for the ESA project QuARL - 21613/08/NL/CB (available from ECMWF, Reading, UK), 49 pp. https://www.ecmwf.int/sites/default/files/elibrary/2009/9438-validation-cloud-parametrization.pdf, last access: 4 September 2025

Gelaro, R., and Coauthors, 2017: The Modern-Era Retrospective Analysis for Research and Applications, Version 2 (MERRA-2). J. Climate, 30, 5419–5454, https://doi.org/10.1175/JCLI-D-16-0758.1.

Gkikas, A., Gialitaki, A., Binietoglou, I., Marinou, E., Tsichla, M., Siomos, N., Paschou, P., Kampouri, A., Voudouri, K. A., Proestakis, E., Mylonaki, M., Papanikolaou, C.-A., Michailidis, K., Baars, H., Straume, A. G., Balis, D., Papayannis, A., Parrinello, T., and Amiridis, V.: First assessment of Aeolus Standard Correct Algorithm particle backscatter coefficient retrievals in the eastern Mediterranean, Atmos. Meas. Tech., 16, 1017–1042, https://doi.org/10.5194/amt-16-1017-2023, 2023.

Gumber, A., Reid, J. S., Holz, R. E., Eck, T. F., Hsu, N. C., Levy, R. C., Zhang, J., and Veglio, P.: Assessment of severe aerosol events from NASA MODIS and VIIRS aerosol products for data assimilation and climate continuity, Atmos. Meas. Tech., 16, 2547–2573, https://doi.org/10.5194/amt-16-2547-2023, 2023.

Haarig, M., Ansmann, A., Baars, H., Jimenez, C., Veselovskii, I., Engelmann, R., and Althausen, D.: Depolarization and lidar ratios at 355, 532, and 1064 nm and microphysical properties of aged tropospheric and stratospheric Canadian wildfire smoke, Atmos. Chem. Phys., 18, 11847–11861, https://doi.org/10.5194/acp-18-11847-2018, 2018.

Haarig, M., Engelmann, R., Baars, H., Gast, B., Althausen, D., and Ansmann, A.: Discussion of the spectral slope of the lidar ratio between 355 and 1064 nm from multiwavelength Raman lidar observations, Atmos. Chem. Phys., 25, 7741–7763, https://doi.org/10.5194/acp-25-7741-2025, 2025.

Haarig, M., Baars, H., König, L., Donovan, D. P., Ansmann, A., Khaykin, S., et al. (2026). The life cycle of a stratospheric smoke plume as seen from EarthCARE—tracking a plume from Canada to Europe. Geophysical Research Letters, 53, e2025GL119977. https://doi.org/10.1029/2025GL119977.

Hu, Q., Goloub, P., Veselovskii, I., and Podvin, T.: The characterization of long-range transported North American biomass burning plumes: what can a multi-wavelength Mie–Raman-polarization-fluorescence lidar provide?, Atmos. Chem. Phys., 22, 5399–5414, https://doi.org/10.5194/acp-22-5399-2022, 2022.

Hunt, W. H., D. M. Winker, M. A. Vaughan, K. A. Powell, P. L. Lucker, and C. Weimer, 2009: CALIPSO Lidar Description and Performance Assessment. J. Atmos. Oceanic Technol., 26, 1214–1228, https://doi.org/10.1175/2009JTECHA1223.1.

Kim, M.-H., Omar, A. H., Tackett, J. L., Vaughan, M. A., Winker, D. M., Trepte, C. R., Hu, Y., Liu, Z., Poole, L. R., Pitts, M. C., Kar, J., and Magill, B. E.: The CALIPSO version 4 automated aerosol classification and lidar ratio selection algorithm, Atmos. Meas. Tech., 11, 6107–6135, https://doi.org/10.5194/amt-11-6107-2018, 2018.

Kirchmeier-Young, M. C., Gillett, N. P., Zwiers, F. W., Cannon, A. J., and Anslow, F. S.: Attribution of the influence of human-induced climate change on an extreme fire season, Earths Future, 7, 2–10, https://doi.org/10.1029/2018EF001050, 2019.

Khaykin, S., Legras, B., Bucci, S., Sellitto, P., Isaksen, L., Tencé, L., Bekki, S., Bourassa, A., Rieger, L., Zawada, D., Jumelet, J., and Godin-Beekmann, S.: The 2019/20 Australian wildfires gen erated a persistent smoke-charged vortex rising up to 35km al titude, Nature Communications Earth and Environment, 1, 22, https://doi.org/10.1038/s43247-020-00022-5, 2020.

Levy, R. C., Mattoo, S., Munchak, L. A., Remer, L. A., Sayer, A. M., Patadia, F., and Hsu, N. C.: The Collection 6 MODIS aerosol products over land and ocean, Atmos. Meas. Tech., 6, 2989–3034, https://doi.org/10.5194/amt-6-2989-2013, 2013.

Liu H, Remer L A, Huang J, et al. Preliminary evaluation of S-NPP VIIRS aerosol optical thickness[J]. Journal of Geophysical Research: Atmospheres, 2014, 119(7): 3942-3962.

Lohmann, U. and Neubauer, D.: The importance of mixed-phase and ice clouds for climate sensitivity in the global aerosol–climate model ECHAM6-HAM2, Atmos. Chem. Phys., 18, 8807–8828, https://doi.org/10.5194/acp-18-8807-2018, 2018.

Lux, O., Lemmerz, C., Weiler, F., Marksteiner, U., Witschas, B., Rahm, S., Geiß, A., and Reitebuch, O.: Intercomparison of wind observations from the European Space Agency's Aeolus satellite mission and the ALADIN Airborne Demonstrator, Atmos. Meas. Tech., 13, 2075–2097, https://doi.org/10.5194/amt-13-2075-2020, 2020.

Mamouri, R.-E., Ansmann, A., Ohneiser, K., Knopf, D. A., Nisantzi, A., Bühl, J., Engelmann, R., Skupin, A., Seifert, P., Baars, H., Ene, D., Wandinger, U., and Hadjimitsis, D.: Wildfire smoke triggers cirrus formation: lidar observations over the eastern Mediterranean, Atmos. Chem. Phys., 23, 14097–14114, https://doi.org/10.5194/acp-23-14097-2023, 2023.

Nicolae, D., A.Nemuc, D.Müller, C.Talianu, J.Vasilescu, L.Belegante, and A.Kolgotin (2013), Characterization of fresh and aged biomass burning events using multiwavelength Raman lidar and mass spectrometry, J. Geophys. Res. Atmos., 118, 2956–2965, doi:10.1002/jgrd.50324.

Nicolae, D., Ciocan, G.-A., Nemuc, A., Nicolae, V., Talianu, C., Vasilescu, J., Dandocsi, A., Radu, C., Cazacu, M.-M., Vulturescu, V., and Belegante, L.: Examining the characteristics of aerosols: a statistical analysis based on a decade of lidar and photometer observations at the Eastern border of ACTRIS, Atmos. Meas. Tech., 19, 1179–1199, https://doi.org/10.5194/amt-19-1179-2026, 2026.

Ohneiser, K., Ansmann, A., Kaifler, B., Chudnovsky, A., Barja, B., Knopf, D. A., Kaifler, N., Baars, H., Seifert, P., Villanueva, D., Jimenez, C., Radenz, M., Engelmann, R., Veselovskii, I., and Zamorano, F.: Australian wildfire smoke in the stratosphere: the decay phase in 2020/2021 and impact on ozone depletion, Atmos. Chem. Phys., 22, 7417–7442, https://doi.org/10.5194/acp-22-7417-2022, 2022.

Ohneiser, K., Ansmann, A., Witthuhn, J., Deneke, H., Chudnovsky, A., Walter, G., and Senf, F.: Self-lofting of wildfire smoke in the troposphere and stratosphere: simulations and space lidar observations, Atmos. Chem. Phys., 23, 2901–2925, https://doi.org/10.5194/acp-23-2901-2023, 2023.

Omar, A. H., Winker, D. M., Kittaka, C., Vaughan, M. A., Liu, Z., Hu, Y., Trepte, C. R., Rogers, R. R., Ferrare, R. A., Lee, K.-P., Kuehn, R. E., and Hostetler, C. A.: The CALIPSO Automated Aerosol Classification and Lidar Ratio Selection Algorithm, J. Atmos. Ocean. Tech., 26, 1994–2014, https://doi.org/10.1175/2009JTECHA1231.1, 2009.

Pappalardo, G., Amodeo, A., Apituley, A., Comeron, A., Freudenthaler, V., Linné, H., Ansmann, A., Bösenberg, J., D'Amico, G., Mattis, I., Mona, L., Wandinger, U., Amiridis, V., Alados-Arboledas, L., Nicolae, D., and Wiegner, M.: EARLINET: towards an advanced sustainable European aerosol lidar network, Atmos. Meas. Tech., 7, 2389–2409, https://doi.org/10.5194/amt-7-2389-2014, 2014.

Paschou, P., Siomos, N., Tsekeri, A., Louridas, A., Georgoussis, G., Freudenthaler, V., Binietoglou, I., Tsaknakis, G., Tavernarakis, A., Evangelatos, C., von Bismarck, J., Kanitz, T., Meleti, C., Marinou, E., and Amiridis, V.: The eVe reference polarisation lidar system for the calibration and validation of the Aeolus L2A product, Atmos. Meas. Tech., 15, 2299–2323, https://doi.org/10.5194/amt-15-2299-2022, 2022.

Peterson, D.A., Fromm, M.D., McRae, R.H.D. et al. Australia’s Black Summer pyrocumulonimbus super outbreak reveals potential for increasingly extreme stratospheric smoke events. npj Clim Atmos Sci 4, 38 (2021). https://doi.org/10.1038/s41612-021-00192-9.

Reitebuch, O.: The Spaceborne Wind Lidar Mission ADM-Aeolus, in: Atmospheric Physics, Research Topics in Aerospace, edited by: Schumann, U., ISBN 978-3-642-30182-7, Springer-Verlag Berlin Heidelberg, 815–827, https://doi.org/10.1007/978-3-642-30183-4_49, 2012.

Rennie, M., Tan, D., Andersson, E., Poli, P., Dabas, A., de Kloe, J., Marseille, G., and Stoffelen, A.: Aeolus Level-2B Algorithm Theoretical Basis Document, version 3.40, https://earth.esa.int/documents/d/earth-online/aeolus_l2b_algorithm_tbd-pdf (last access: 28 August 2025), 2020.

Savtchenko A, Ouzounov D, Ahmad S, et al. Terra and Aqua MODIS products available from NASA GES DAAC[J]. Advances in Space Research, 2004, 34(4): 710-714.

Shang, X., Lipponen, A., Filioglou, M., Sundström, A.-M., Parrington, M., Buchard, V., Darmenov, A. S., Welton, E. J., Marinou, E., Amiridis, V., Sicard, M., Rodríguez-Gómez, A., Komppula, M., and Mielonen, T.: Monitoring biomass burning aerosol transport using CALIOP observations and reanalysis models: a Canadian wildfire event in 2019, Atmos. Chem. Phys., 24, 1329–1344, https://doi.org/10.5194/acp-24-1329-2024, 2024.

Sokolik, I. N., Soja, A. J., DeMott, P. J., and Winker, D: Progress and challenges in quantifying wildfire smoke emissions, their properties, transport, and atmospheric impacts, J. Geophys. Res. Atmos., 124, 13005–13025. https://doi.org/10.1029/2018JD029878, 2019.

Song, R., Povey, A., and Grainger, R. G.: Characterization of dust aerosols from ALADIN and CALIOP measurements, Atmos. Meas. Tech., 17, 2521–2538, https://doi.org/10.5194/amt-17-2521-2024, 2024.

Stein, A.F., Draxler, R.R, Rolph, G.D., Stunder, B.J.B., Cohen, M.D., and Ngan, F., (2015). NOAA's HYSPLIT atmospheric transport and dispersion modeling system, Bull. Amer. Meteor. Soc., 96, 2059-2077, http://dx.doi.org/10.1175/BAMS-D-14-00110.1.

Stoffelen, A., Pailleux, J., Källén, E., Vaughan, J. M., Isaksen, L., Flamant, P., Wergen, W., Andersson, E., Schyberg, H., Culoma, A., Meynart, R., Endemann, M., and Ingmann, P.: The Atmospheric Dynamics Mission For Global Wind Field Measurement, B. Am. Meteorol. Soc., 86, 73–88, https://doi.org/10.1175/BAMS-86-1-73, 2005.

Tan, D. G., Andersson, E., Kloe, J. D., Marseille, G.-J., Stoffelen, A., Poli, P., Denneulin, M.-L., Dabas, A., Huber, D., and Reitebuch, O.: The ADM-Aeolus wind retrieval algorithms, Tellus A, 60, 191–205, https://doi.org/10.1111/j.1600-0870.2007.00285.x, 2008.

Trapon, D., Baars, H., Floutsi, A. A., Bley, S., Haarig, M., Lacour, A., Flament, T., Dabas, A., Nehrir, A. R., Ehlers, F., and Huber, D.: Cross-validations of the Aeolus aerosol products and new developments with airborne high-spectral-resolution lidar measurements above the tropical Atlantic during JATAC, Atmos. Meas. Tech., 18, 3873–3896, https://doi.org/10.5194/amt-18-3873-2025, 2025.

Trickl, T., Vogelmann, H., Fromm, M. D., Jäger, H., Perfahl, M., and Steinbrecht, W.: Measurement report: Violent biomass burning and volcanic eruptions – a new period of elevated stratospheric aerosol over central Europe (2017 to 2023) in a long series of observations, Atmos. Chem. Phys., 24, 1997–2021, https://doi.org/10.5194/acp-24-1997-2024, 2024.

Twohy, C. H., Toohey, D. W., Levin, E. J. T., DeMott, P. J., Rainwater, B., Garofalo, L. A., Pothier, M. A., Farmer, D. K., Kreidenweis, S. M., Pokhrel, R. P., Murphy, S. M., Reeves, J. M., Moore, K. A., and Fischer, E. V.: Biomass burning smoke and its influence on clouds over the western U. S., Geophys. Res. Lett., 48, e2021GL094224. https://doi.org/10.1029/2021GL094224, 2021.

~~Twohy, C. H., Toohey, D. W., Levin, E. J. T., DeMott, P. J., Rainwater, B., Garofalo, L. A., et al. (2021). Biomass burning smoke and its influence on clouds over the western U. S. *Geophysical Research Letters*, 48, e2021GL094224. https://doi.org/10.1029/2021GL094224~~

Vaughan, G., Draude, A. P., Ricketts, H. M. A., Schultz, D. M., Adam, M., Sugier, J., and Wareing, D. P.: Transport of Canadian forest fire smoke over the UK as observed by lidar, Atmos. Chem. Phys., 18, 11375–11388, https://doi.org/10.5194/acp-18-11375-2018, 2018.

Wang, P., Donovan, D. P., van Zadelhoff, G.-J., de Kloe, J., Huber, D., and Reissig, K.: Evaluation of Aeolus feature mask and particle extinction coefficient profile products using CALIPSO data, Atmos. Meas. Tech., 17, 5935–5955, https://doi.org/10.5194/amt-17-5935-2024, 2024.

Winker, D. M., Vaughan, M. A., Omar, A. H., Hu, Y., Powell, K. A., Liu, Z., Hunt, W. H., and Young, S. A.: Overview of the CALIPSO Mission and CALIOP Data Processing Algorithms, J. Atmos. Ocean. Technol., 26, 2310–2323, 2009.